AGU PUBLICATIONS

JGR

Journal of Geophysical Research: Earth Surface

RESEARCH ARTICLE

10.1002/2014JF003359

Key Points:
- Mass flux is most sensitive to basal drag
- Mass flux is the most uncertain at the 79North outlet
- Geothermal heat flux uncertainty is less than that from cryohydrologic warming

Correspondence to:
N.-J. Schlegel,
nschlegel@gmail.com

Citation:
Schlegel, N.-J., E. Larour, H. Seroussi, M. Morlighem, and J. E. Box (2015), Ice discharge uncertainties in Northeast Greenland from boundary conditions and climate forcing of an ice flow model, *J. Geophys. Res. Earth Surf.*, *120*, 29–54, doi:10.1002/2014JF003359.

Received 2 OCT 2014
Accepted 8 DEC 2014
Accepted article online 11 DEC 2014
Published online 15 JAN 2015

Ice discharge uncertainties in Northeast Greenland from boundary conditions and climate forcing of an ice flow model

N.-J. Schlegel[1], E. Larour[1], H. Seroussi[1], M. Morlighem[2], and J. E. Box[3]

[1]Jet Propulsion Laboratory, California Institute of Technology, Pasadena, California, USA, [2]Department of Earth System Science, University of California, Irvine, California, USA, [3]Geological Survey of Denmark and Greenland, Copenhagen, Denmark

Abstract In order to understand ice sheet response to climate change, it is critical to examine errors associated with ice flow model boundary conditions and forcing. It is also important to understand how these errors propagate through numerical ice sheet models and contribute to uncertainty in model output. Using established uncertainty quantification methods within the Ice Sheet System Model (ISSM), we investigate the sensitivity of ice flow within the Northeast Greenland Ice Stream (NEGIS) to key fields, including ice viscosity and basal drag, and compare them with model sensitivity to climate forcing. In addition, we examine how errors in model input manifest as mass flux uncertainties during a forward simulation of the NEGIS from 1989 to 2010. Overall, we find that mass flux is most uncertain in the main outlets, Nioghalvfjerdsbræ and Zachariæ Isstrøm, and that mass flux is most sensitive to basal drag, though errors associated with basal drag are poorly constrained and difficult to quantify. Given our knowledge of errors associated with the thermal properties of ice, we estimate that in the ablation area, the effects of cryohydrologic warming contribute over 4 times more mass flux uncertainty that do errors in geothermal heat flux. We find that NEGIS total ice discharge is associated with a 0.7 Gt/yr (2.6%) uncertainty due to errors in geothermal heat flux and a 3.3 Gt/yr (11.6%) uncertainty due to the added effects of cryohydrologic warming. In comparison, errors in surface mass balance contribute 4.5 Gt/yr to NEGIS total discharge uncertainty.

1. Introduction

The Greenland Ice Sheet is amongst the largest contributors to sea level rise [*Gardner et al.*, 2013; *Intergovernmental Panel on Climate Change*, 2013], and observations indicate that its rate of ice loss has accelerated by more than 25 Gt/yr^2 during the last decade [*Wouters et al.*, 2013; *Enderlin et al.*, 2014]. Recent studies have suggested that on average, 60% of this acceleration can be attributed to greater surface melt [*Enderlin et al.*, 2014], and 40% to ice dynamics at the ice sheet margins [*Rignot et al.*, 2008; *van den Broeke et al.*, 2009; *Sasgen et al.*, 2012]. Increased melt, both on the surface and at the ice-ocean interface, is likely responsible for submonthly-to-decadal-scale changes in ice flow, including lubrication of the glacial bed [*Bartholomew et al.*, 2010; *Schoof*, 2010; *Tedesco et al.*, 2012], warming of the glacial ice due to surface melt-water drainage and refreeze at depth [*Pfeffer et al.*, 1991; *Fausto et al.*, 2009; *Phillips et al.*, 2013; *Bell et al.*, 2014], increased runoff into the ocean [*Hanna et al.*, 2008], grounding line retreat [*Rignot et al.*, 2010; *Holland et al.*, 2008], and changes to flow resistance at the calving front [*Walter et al.*, 2012].

Overall, the understanding of these processes and their interactions is incomplete, and it is difficult to pinpoint which of these processes is most responsible for observed changes in ice flow. A lack of comprehensive spatial and temporal observational coverage over the majority of ice sheet [*Bales et al.*, 2009; *Ettema et al.*, 2009; *Burgess et al.*, 2010] contributes to this shortcoming, especially because simulations of ice sheet flow require input of high spatial and temporal resolution, and observations are often sparse. In addition, ice sheet models vary in their treatment of key processes (i.e., assumptions during initialization, implementation of model forcing, choice of flow equations and sliding laws, etc.). Such differences lead to a significant spread in model behavior and ice flow response to climate forcing [*Nowicki et al.*, 2013]. As a result, projections of Greenland's sensitivity to climate change vary dramatically and are largely uncertain.

Model uncertainties are mainly rooted in input errors including temperature regime (i.e., ice viscosity, surface temperature, and geothermal heat flux), surface velocity and elevation, ice thickness, ice front position, and surface mass balance (SMB). While surface observations, including velocities [e.g., *Rignot and Mouginot*,

2012], elevation [e.g., *Schenk and Csatho*, 2012], and SMB [e.g., *Box*, 2013], are relatively well known, thermal properties (i.e., temperature, geothermal heat flux, and ice viscosity) are among the most poorly constrained [*Seroussi et al.*, 2013]. This is partly due to the availability of only a limited number of deep ice cores [e. g., *Greenland Ice-Core Project (Grip) Members*, 1993; *Dansgaard et al.*, 1993; *Dahl-Jensen et al.*, 2013], which offer the most valuable information about the internal thermal properties of the ice sheet. In addition, geothermal heat flux itself is highly uncertain. For instance, various model estimates, including tectonic [*Pollack et al.*, 1993], seismic [*Shapiro and Ritzwoller*, 2004], and magnetic [*Fox Maule et al.*, 2009] solutions find little agreement. As a boundary condition of an ice sheet model, the geothermal heat flux impacts estimates of ice viscosity and basal drag and in turn affects characteristics of ice flow [*Larour et al.*, 2012a; *Seroussi et al.*, 2013].

In this study, we use uncertainty quantification (UQ) to investigate how local ice flow is affected by errors in various model input [*Larour et al.*, 2012b, 2012a]. UQ tools are provided by the Ice Sheet System Model (ISSM) and supported by the Design Analysis Kit for Optimization and Terascale Applications (Dakota) software. They rely on Monte Carlo-style sampling methods to derive uncertainties in model output, given specified errors in the model inputs. *Larour et al.* [2012b] were the first to use the ISSM-Dakota framework to compare the relative sensitivities of steady state stress balance solutions of Pine Island Glacier, West Antarctica, to ice thickness, ice viscosity, and basal drag. They later investigated Pine Island Glacier's mass flux sensitivity to geothermal heat flux [*Larour et al.*, 2012a], concluding that errors in initial ice thicknesses contribute most to uncertainties in steady state stress balance solutions of fast-flowing ice streams near the margins. *Schlegel et al.* [2013] used UQ to investigate the impact of SMB errors on a transient decadal-scale simulation of Northeast Greenland. Here we aim to compare these past results with uncertainties due to model initial boundary conditions (i.e., basal drag and geothermal heat flux) and climate-driven changes to the thermal ice regime. Recently, *Seroussi et al.* [2013] investigated the continental-scale effects of these boundary conditions on 100 year model estimates of Greenland's contribution to sea level rise using parameter-space studies and concluded that basal drag and climate forcing have a stronger effect on Greenland mass balance than does the thermal ice regime. For this study, we utilize UQ tools to further understand how errors in different model inputs affect decadal-scale ice flow and mass outflux within one of the most dynamically active regions of Greenland.

Our region of interest, Northeast Greenland, is distinguished by a fast-flowing ice stream that stretches 600 km upstream of three major outlet glaciers [*Fahnestock et al.*, 2001; *Joughin et al.*, 2001]. This area is of interest particularly because of marginal thinning recently captured by observations and the regional potential for dynamic drawdown of ice from Greenland's interior [*Khan et al.*, 2014]. Model estimates of geothermal heat flux in this area vary substantially by more than 200% [e.g., *Shapiro and Ritzwoller*, 2004; *Fox Maule et al.*, 2009]. Such differences in geothermal flux boundary conditions result in varying estimates of the ice sheet's thermal regime. These inconsistencies propagate through an ice sheet model, resulting in uncertainties in modeled ice flow [*Greve and Hutter*, 1995; *Greve*, 2005; *Rogozhina et al.*, 2012]. Other sources of uncertainty in ice flow models include missing processes, particularly those associated with the runoff of surface meltwater. Surface meltwater within the ablation area finds its way through crevasses in the ice, penetrating through the entire ice column [*Phillips et al.*, 2013; *Bell et al.*, 2014]. It then refreezes and releases heat into the ice sheet [*Cuffey and Paterson*, 2010]. This process, known as cryohydrologic (CH) warming, is capable of increasing the temperature of an ice column by more than 10°C, resulting in notable enhancement in ice fluidity [*Phillips et al.*, 2010, 2013]. ISSM does not model the effects of CH refreeze on ice viscosity. Nor does it consider the enhancement of basal sliding where meltwater reaches the bed [*Bartholomew et al.*, 2010; *Schoof*, 2010], even though observational evidence suggests that these processes are associated with the onset of fast flow. These missing processes introduce errors into the ice flow model and ultimately contribute to uncertainties in model estimates of ice discharge into the ocean. In this study we assess such errors and use the ISSM-Dakota framework to quantify their effects on mass flux uncertainty at three major outlet glaciers, Nioghalvfjerdsbræ (79North), Zachariæ Isstrøm, and Storstrømmen glacier, and in the upper branches of the Northeast Greenland Ice Stream (NEGIS) that feed these glaciers. To do so, we consider a transient model of the NEGIS, forced with annual SMB and run for 22 years, from 1 January 1989 to 31 December 2010.

In section 1 of this study, we describe the ice flow model and the treatment of ice dynamics, thermal properties, and basal drag, as well as the methods used for UQ. In section 2, we describe the model setup, the data sets used for initialization, boundary conditions, forcing, and associated errors. In sections 3 and 4,

we present UQ results, focusing on the comparison between the mass flux uncertainties driven by different sources of error in model boundary conditions that may propagate in a forward model on decadal time scales. Finally, we conclude by discussing how each field affects model dynamics and what the resulting sensitivities suggest about the relative importance of each field to the accuracy of ice stream simulations.

2. Model

ISSM is a thermomechanical finite-element ice flow model. It relies upon the conservation laws of momentum, mass, and energy, combined with constitutive material laws and boundary conditions. The implementation of these laws and treatment of model boundary conditions are described by *Larour et al.* [2012c]. Below, we review the ice sheet model components pertinent to this study, namely, the stress balance, mass transport, and thermal models.

2.1. Ice Flow Model

Here we simulate the fast-flowing NEGIS on a high-resolution mesh, with a two-dimensional (2-D) Shelfy-Stream Approximation (SSA) [*MacAyeal*, 1989], implemented within ISSM [*Larour et al.*, 2012c]. The SSA is based on the Stokes equations and assumes that vertical shear and bridging effects are negligible. These assumptions reduce the momentum balance equation to the desired 2-D system equations. The SSA is well suited for the NEGIS [*Schlegel et al.*, 2013], which has high-velocity flow, dominated by basal sliding [*Joughin et al.*, 2001]. The SSA is computationally efficient compared to higher-order models, which is an advantage for running UQ methods that require a large number of samples to be run affordably [*Larour et al.*, 2012b]. Below, we describe how ice flow simulated with SSA is affected by the various fields of interest in this study.

For the 2-D SSA model, ice flow is governed by the nonlinear depth-averaged effective ice viscosity η as follows:

$$\eta = \frac{B}{2\,\dot{\varepsilon}_e^{\frac{n-1}{n}}} \tag{1}$$

where B is the depth-averaged ice viscosity parameter, n Glen's law exponent, and $\dot{\varepsilon}_e$ the effective strain rate [*Glen*, 1955]. B is temperature dependent, based on best fit cubic spline between the depth-averaged temperature and recommended values of B from *Paterson* [1994, p. 97]. In the 2-D model, B is determined by vertically averaging the thermal steady state ice temperatures. During all forward runs, ice temperatures, and therefore B, remain fixed through time.

In order to determine ice temperatures, we calculate a thermal steady state condition for the ice sheet. Our thermal model, described in *Larour et al.* [2012c], includes advection and diffusion in all three directions. Three-dimensional (3-D) transport velocities are calculated using a stress balance model, forced by observed surface velocities and an initial estimate of basal drag. In order to determine a thermal steady state, these conditions are assumed constant, resulting in the simplified steady state energy equation:

$$\rho c\, \mathbf{v} \cdot \nabla T = k_{\text{th}} \Delta T + \Phi \tag{2}$$

where T is the temperature of ice, $\mathbf{v}$ the velocity vector, k_{th} the ice thermal conductivity, c the ice heat capacity, Φ the deformational heating, ρ the ice density, Δ the Laplace operator, and ∇ the gradient operator.

At the surface boundary of the thermal model, temperature is prescribed as a Dirichlet boundary condition, equal to mean surface air temperature. At the base, the following heat flux is applied through a Neumann boundary condition:

$$k_{\text{th}} \nabla T \cdot \mathbf{n} = G - \boldsymbol{\tau}_b \cdot \mathbf{v}_\mathbf{b} \tag{3}$$

where $-\boldsymbol{\tau}_b \cdot \mathbf{v}_\mathbf{b}$ is the heat generated by friction at the base, $\mathbf{v}_\mathbf{b}$ is the basal velocity vector tangential to the glacier base plane, $\boldsymbol{\tau}_b$ the tangential component of the external force $\boldsymbol{\sigma} \cdot \mathbf{n}$, G the geothermal heat flux, and $\mathbf{n}$ the normal vector to the ice-bedrock interface. The fields $\boldsymbol{\tau}_b$ and $\mathbf{v}_\mathbf{b}$ are related as follows:

$$\boldsymbol{\tau}_b = -\alpha^2 N \mathbf{v}_\mathbf{b} \tag{4}$$

where α is defined as an empirically derived basal drag coefficient [*Cuffey and Paterson*, 2010] and N is the effective pressure of the water at the glacier base. Since the calculation of effective pressure requires a full hydrological model not yet available in ISSM, it is approximated by $N = g(\rho H + \rho_w z_b)$ [*Cuffey and Paterson*, 2010], where H is ice thickness, ρ_w is the density of water, g is gravity, and z_b is bedrock elevation relative to sea level. Here z_b is equal to zero at sea level and negative below sea level. In ISSM, during a forward run, the ice sheet geometry changes with time, and the values of H and N are updated accordingly. At the ice-sea water interface, depth-integrated water pressure is imposed. On all other boundaries where stresses are not specified, Dirichlet boundary conditions equal to observed velocities are prescribed. The determination of the parameter α relies on inverse methods [*MacAyeal*, 1993], following *Morlighem et al.* [2010], where we choose the spatially varying α field required to match interferometric synthetic aperture radar (InSAR) surface velocities.

During forward simulations of the Greenland continental model, only SMB is forced through time. During forward simulations of the regional model, we impose Dirichlet boundary conditions for ice velocity and thickness at all ice-ice interfaces. Velocities everywhere else on the domain are allowed to evolve freely during the forward run. The model does not include bedrock deformation or migrating boundaries, thus the bed geometry and the ice front position are imposed and fixed in time. Throughout the simulation, all ice is assumed to be grounded. Changes in SMB are communicated to the ice flow through the mass transport model, which is driven by mass conservation as follows:

$$\frac{\partial H}{\partial t} = \dot{M}_s - \nabla \cdot H\bar{\mathbf{v}} \tag{5}$$

where $\bar{\mathbf{v}} = (\bar{u}, \bar{v})$ is the vertically averaged horizontal velocity and $\dot{M}_s$ the surface mass balance (m/yr ice equivalent).

2.2. Uncertainty Quantification

Uncertainty quantification (UQ) is a nondeterministic analysis used to characterize how input errors forward propagate through a computational model, with the ultimate goal of statistically assessing how errors and assumptions affect model outputs or results. ISSM UQ methods are based on the Dakota software [*Eldred et al.*, 2008]. The Dakota-based UQ methods focus specifically on the forward propagation of input errors. Dakota is responsible for taking given probabilistic or interval information on inputs and mapping them through the computational model by repeatedly running the same model many times. With each run, the model is perturbed, and the resulting collection of model results is used to assess statistics or intervals on model outputs. These types of forward analyses are computationally demanding, so it is advantageous to run a simple, highly efficient simulation that is also capable of capturing the intended model physics.

Dakota UQ methods used in this study include sampling and sensitivity analyses. We respectively rely on these analyses to (1) identify how variations in model fields impact uncertainty in NEGIS ice flow and (2) understand the sensitivity of NEGIS ice flow to local variations in model fields. These analyses are carried out on equal area partitions of the model domain in order to remove area-specific dependencies (see section 3.3.2).

The first type of UQ, *sampling analysis*, quantifies how input errors propagate through a model to impact specified model output. It is a Monte Carlo style methodology that relies on repeated execution of the same model or samples, where input variables are perturbed by different amounts at each partition for each individual run. Input values are perturbed randomly within a prescribed range (described by a statistical distribution, e.g., normal or uniform), separately for each partition. Resulting statistics, including means, standard deviations, and cumulative distribution functions, are calculated after all the sample runs are completed.

By definition, normal distributions cluster around μ and decrease toward the tails in a Gaussian bell curve, where 99.73% of the data fall within $\mu \pm 3\sigma$. For uniform distributions, probability of occurrence is equal for any given value within a given range around the average, μ. In this study, we sample the ice viscosity parameter using a uniform distribution, because errors are inferred from difference margins between two model solutions (see section 3.3.2). For the basal drag coefficient and SMB, we sample using a normal distribution.

For each sample, we determine the value of the model perturbation as follows. At the beginning of a sample run for a particular field ($\mathcal{F}$), the Dakota software chooses random percentage perturbation P_i at each

partition i that falls within a normal or uniform distribution such that

$$\mu_i = 1$$
$$\sigma_i = \frac{e_i}{|\mathcal{F}(i)|} \tag{6}$$

where μ_i is the average value of the distribution scaled to 1, σ_i is the corresponding scaled standard deviation, and e_i is the standard error. Generation of the P_i values relies on a binned Latin Hypercube Sampling algorithm [*Swiler and Wyss*, 2004], and P_i remains constant for every partition over the duration of each transient simulation. In the case that we sample multiple fields at the same time, a random P_i is chosen separately for each field (as described above) before each sample run, and mass flux uncertainty is determined as the effect of the combined input errors.

We perturb the ice viscosity parameter and the basal drag coefficient, which are time constant fields, by $\mathcal{F}P_i$ during the entire simulation. Because SMB is a function of time, we set σ_i equal to the time mean of the σ_i values (Note that this varies from the methods in *Schlegel et al.* [2013], where σ_i was calculated as the fraction between e_i and the mean 1989–2010 SMB.). This means, in the case of SMB, at a particular time step t, we perturb the SMB value by $\dot{M}_s(t)P_i$.

The second type of UQ, *sensitivity analysis*, computes the local derivative of model output with respect to a model field. The spatial distribution of this derivative is assessed for the purpose of comparing how various inputs affect flow in different locations throughout the domain. Using the established ISSM framework, we quantify how the location of errors impact mass flux through a specified flux gate by imposing a small change in a model field to each partition separately. Once a partition is perturbed for a particular field, one transient run is performed and a sensitivity is assigned to that partition. This is done for every partition and every field, resulting in one transient simulation per field per partition. Mass flux responses are determined at the completion of each simulation.

Sensitivity value, θ_i, represent the magnitude of output response to a 0.1% input perturbation at each partition i. Therefore, within a particular partition, the perturbed value becomes $1.001\mathcal{F}(i)$. It is important to note that because values are perturbed by a percentage, perturbed SMB becomes more negative in the ablation area but more positive in the accumulation area.

In addition, we use the sensitivity values to calculate maps of scaled sensitivities, SS_i, which we define as follows:

$$SS_i = \frac{\theta_i^2}{\sum_{i=1}^{m} \theta_i^2} \tag{7}$$

where m is the number of domain partitions. Scaled sensitivities nondimensionally represent the relative contributions of sensitivities throughout the domain. Since SS values over the entire domain sum to unity, they can be used to compare the relative contribution of different model fields.

Finally, after *Schlegel et al.* [2013], we use the SS values to calculate radii of influence for all fields of interest. The radius of influence is defined as the maximum distance between a flux gate and all locations with SS values that are less than a given magnitude. Such values allow us to quantify for each field, the length-scale of its first-order influence on a given flux gate.

3. Methods

3.1. Model Forcing

The ISSM Greenland setup and initialization is described in detail by *Schlegel et al.* [2013]. For the continental model, the anisotropic mesh is made up of 72,320 elements, refined using observed surface [*Scambos and Haran*, 2002] and velocity [*Rignot and Mouginot*, 2012] fields. Mesh resolution ranges from 1 km at steep areas with high-velocity gradients to 15 km at the ice divide. The bedrock geometry is initialized using a 150 m gridded bedrock data from *Morlighem et al.* [2014]. Annual SMB forcing is provided by *Box* [2013]. The SMB time series is interpolated from 5 km yearly grids [*Box et al.*, 2013; *Box*, 2013] and is imposed yearly through a one-way coupling scheme [*Schlegel et al.*, 2013]. For consistency with this SMB forcing, we use the ice surface from *Scambos and Haran* [2002].

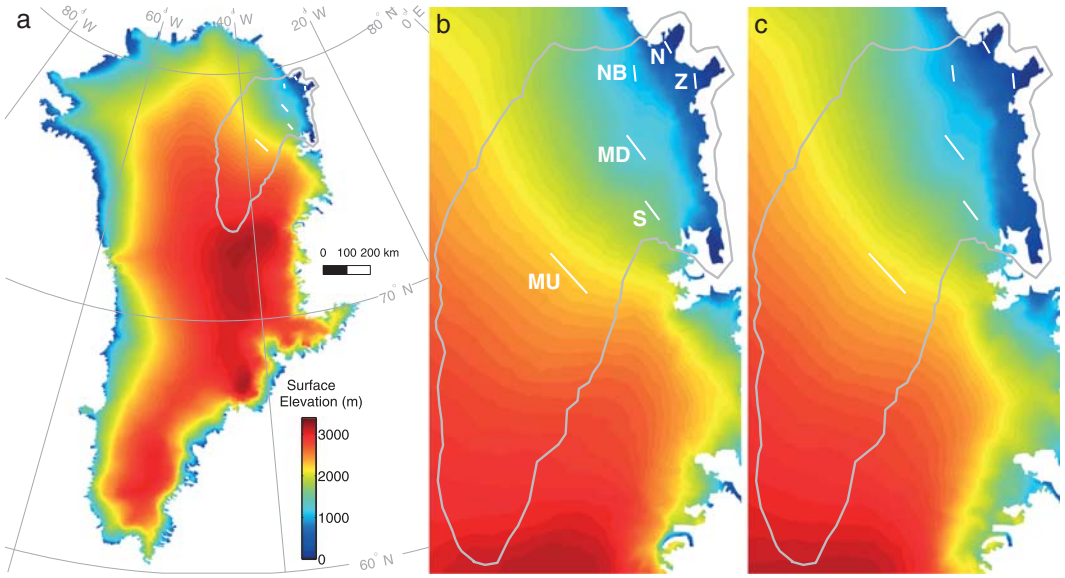

Figure 1. Modeled ice surface elevation after relaxation for (a) the entire ice sheet and (b) the NEGIS. The NEGIS regional model domain is outlined in gray. Also shown are the six mass flux gates assessed for UQ (white lines): one each across 79North (Gate N), Zachariæ Isstrøm (Gate Z), and Storstrømmen (Gate S) outlets; one across the northern branch (Gate NB); and two across the main branch, one downstream (Gate MD) and one upstream (Gate MU). For comparison, we include (c) observed surface elevation from *Scambos and Haran* [2002].

For thermal steady state, we use surface temperatures from *Ettema et al.* [2009] and geothermal heat flux from *Shapiro and Ritzwoller* [2004]. For the inversion, surface velocities are from InSAR [*Rignot and Mouginot*, 2012].

3.2. Relaxation

As done in *Schlegel et al.* [2013], we run the Greenland model to a steady state condition where the discharge is equal to the total SMB forcing. Here we use an average SMB field from the years 1971 to 1988, since during this period, Greenland's total mass balance was close to zero [*Rignot et al.*, 2008]. Ice temperature is held constant throughout the simulation. Since we are interested in isolated responses to perturbed model fields during a forward model run, we adopt this simple spinup procedure meant to relax the model to a state where it would be in balance during the 1971–1988 period. The steady state ice sheet geometry differs from the observed ice sheet mostly at the margins (Figure 1); below 2000 m elevation the ice surface is on average 100 m thicker and 15 m/yr slower than observations. These changes are responsible for a 3.6% increase in volume after 6000 years of relaxation to a constant climatological forcing.

Next, the forward model is run for 170 years. The model is forced annually from 1841 to 2010. Again, ice temperatures are held constant. The resulting states of the ice sheet (namely, ice thickness, bedrock elevation, and velocities), at the end of year 1988, are the initial conditions for the UQ methods. As described in *Schlegel et al.* [2013], we extract the NEGIS regional domain from the continental ice sheet at the end of year 1988. The new domain consists of all the elements of the Greenland domain that are located within the NEGIS drainage basin (Figure 1), a total of 3711 elements (Figure 2a). We include plots of modeled ice thickness, velocity, and the basal drag coefficient inferred from observed ice velocities within the NEGIS domain (Figures 2b–2d). All ice-ice boundaries are forced through time, with Dirichlet boundary conditions, set equal to the ice velocity and thickness values that result from the continental Greenland transient run.

An analysis of modeled ice flow within the regional NEGIS domain reveals that the largest limits of SSA appear (1) in areas of slow-moving ice along the margins [*Seroussi et al.*, 2011] (affecting the most narrow outlet gates along their profile margins, where there is an intense transition from high-velocity to low-velocity flow) and (2) in the upper part of the ice stream (where vertical shearing is more intense and surface to basal velocity differences reach up to 6% of the depth-averaged velocity) [*Schlegel et al.*, 2013]. However, we find that in areas where the basal drag coefficient has a value of 35 $(m/s)^{-1/2}$ or less (Figure 2d), the average difference between surface and basal velocity is 1% of the depth-averaged velocity. In the 60%

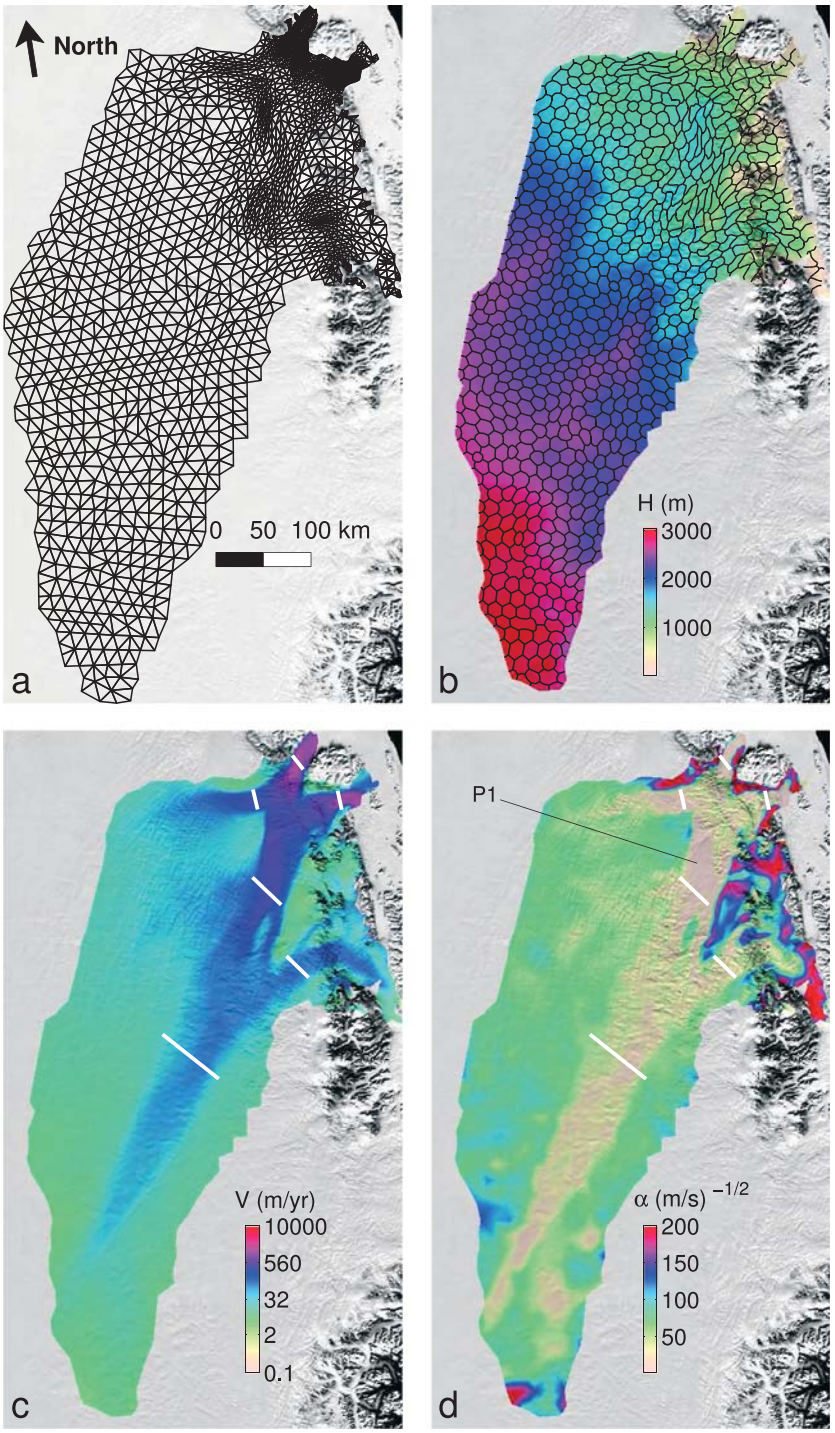

Figure 2. (a) Model mesh, resolution ranging from 1 km at the margins to 15 km at the summit, (b) modeled ice thickness after relaxation and 1000 partitions, (c) modeled velocities after relaxation, and (d) α resulting from inversion. For reference, mass flux gates for UQ (white lines) are also shown, and the location of P1 is highlighted as an area of minimum basal drag. The state of the domain, extracted from the full Greenland domain after relaxation, dictates initial conditions for the 22 year UQ runs.

of the domain area with a basal drag coefficient value of 75 $(m/s)^{-1/2}$ or less, the mean difference is 4% of the depth-averaged velocity. The SSA is therefore a reasonable choice for simulating the high-velocity areas of the NEGIS. However, we expect the ice flow located far upstream and away from the large branches of the NEGIS to be less accurately simulated.

Note that this spinup procedure is idealized for sensitivity studies, and we do not expect the resulting modeled ice sheet to have the same geometry as the actual ice sheet at the end of 1988 [*Schlegel et al.*, 2013]. We assume that the ISSM configuration presented here resembles the state of Greenland 25 years ago and argue that the resulting thermal and velocity regimes of the ice sheet represent reasonable starting conditions for examining ice sensitivity to realistic errors in its forcing and boundary conditions.

3.3. Uncertainty Quantification Methods

The goals of this analysis are to assess the forward propagation of errors in the depth-averaged ice viscosity parameter (B) and the basal drag coefficient (α) in decadal-scale ice flow and to investigate how this differs from the propagation of errors in SMB. For sensitivity studies, we focus on the spatial characteristics and extent of the changes resulting from small perturbations in each of these fields. For sampling studies, we consider how errors in the model fields impact mass fluxes and NEGIS mass balance.

3.3.1. Mesh Partitioning

Using the regional NEGIS domain, we bin the model vertices into equal area partitions using the Chaco: Software for Partitioning Graphs [*Hendrickson and Leland*, 1995]. In Figure 2b we plot the 1000 partitions used for UQ in this study. We choose 1000 partitions in order to capture the outlet glaciers at the finest partition resolution possible. It is important to note, however, that in the higher elevations of the NEGIS domain, the mesh resolution (15 km) is low compared to the resolution at lower elevations (1 km). Figure 2a illustrates the ISSM mesh elements and vertices for the NEGIS region. This discrepancy in mesh resolution restricts Chaco to the designation of only one ISSM mesh vertex per partition at high elevations, while in the faster-flowing regions tens of vertices are assigned to each partition. This is evidenced in the partition outlines in the higher elevations of the domain and should be taken into consideration when focusing on low-resolution areas of the mesh.

3.3.2. Sampling Errors

The first set of B sampling experiments focuses on errors that are attributed to geothermal heat flux, which we refer to as B_g. For the second set of sampling experiments, we consider errors in B that are introduced into the model both by geothermal heat flux and the process of CH warming not simulated by the model [*Phillips et al.*, 2010, 2013; *Bell et al.*, 2014]. For the application of errors associated with the process of CH refreeze and warming, we introduce additional B error into the ablation area. We refer to this new error field (which is equal to B_g in the accumulation area and includes CH refreeze errors only in the ablation area) as B_r. Note that because the simulations are run in 2-D, the B value is depth averaged, so all errors are effectively applied to the entire ice column.

In Figures 3a and 3b, we plot the modeled B field within the regional NEGIS domain and the standard error of B_g used for the sampling analyses. To determine errors in B_g, we rerun the thermal steady state calculation using geothermal heat flux from *Fox Maule et al.* [2009] and calculate 3-D ice viscosity based on the resulting temperatures. We compare these with the 3-D ice viscosity parameter resulting from the steady state calculation using *Shapiro and Ritzwoller* [2004]. On average, the *Fox Maule et al.* [2009] solution varies 17% from the original *Shapiro and Ritzwoller* [2004] solution, with a maximum difference of 35%. For each partition, we take the difference between the two solutions at every mesh vertex and assign the maximum value within the partition, ΔB_i, as our error range in B_g. The B sampling is represented by a uniform distribution centered at the spinup value for B, and we define the total range of the error distribution to be equal to the value of $|\Delta B_i|$.

For sampling of B_r, we adopt a simple representation of error in the ablation area. *Phillips et al.* [2010] suggest that the refreezing of surface meltwater in the ablation area could be responsible for an increase in ice fluidity of 5 times its approximated value. Such a change is equivalent to a 42% change in the ice viscosity parameter B [*Paterson*, 1994]. In order to investigate the magnitude of the uncertainty due to CH warming, we apply this extreme value as error in the ablation area. As a result, for B_r in the ablation area, we set $\Delta B_i = 0.42$, while in accumulation area, errors remain equal to the errors associated with B_g.

Because errors in basal drag are much more difficult to quantify, we choose a normal distribution using constant 3σ error values of 5% and 20% over the domain. These two values are chosen because, on average,

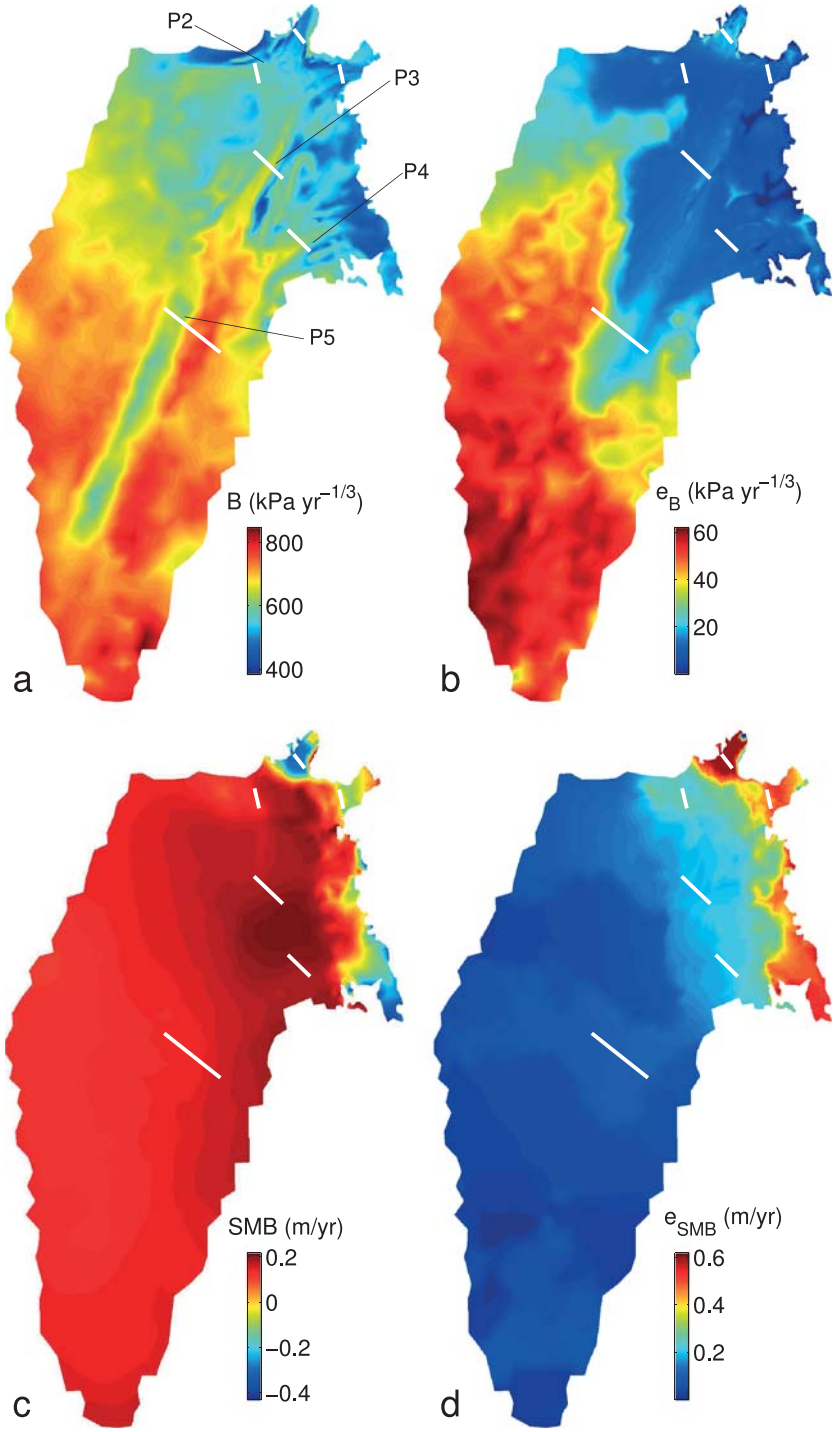

Figure 3. (a) Ice viscosity parameter, *B*, estimated from thermal steady state, with areas of large cross-flow gradients labeled as P2–P5. (b) *B* standard error due to geothermal heat flux (e_B), determined as the standard deviation of a uniform distribution with a total range equal to the difference between the *B* fields achieved when calculating thermal steady state with two different geothermal heat flux maps. For comparison, we also include the following: (c) mean SMB over the sampling period (1989–2010) and (d) SMB standard error (e_{SMB}) in m/yr water equivalent. The six mass flux gates are marked with white lines.

the mass flux uncertainty ranges associated with 5% and 20% errors in α are found to be comparable to mass flux uncertainties for other fields. Ice flow is very sensitive to our choice of α, and it is the model parameter determined by inversion of surface velocities during the model spinup. Here we include the predetermined incremental samples of α in the sampling analysis as references, as we find them useful for comparison, especially when gauging the magnitude of uncertainties against the uncertainties of other fields. For an extreme example of α, we choose a constant 150% 3σ error. For this extreme case, the distribution is uniform, in order to constrain α to positive values.

For comparison with the above fields, we include SMB results [after *Schlegel et al.*, 2013] using a normal distribution. In Figures 3c and 3d, we plot the mean SMB forcing and the standard errors used for SMB sampling. The determination of SMB errors is described in detail in *Schlegel et al.* [2013] [after *Box*, 2013]. Here we present new results for the northern and southern branches of the ice stream. In addition, for the main branch, we present results updated from *Schlegel et al.* [2013]. Updates include a new model spinup with an improved bedrock map [*Morlighem et al.*, 2014] and an increase in the number of sample runs (from 200 to 500).

3.3.3. Execution

To complete the UQ analysis, we force our partitioned, regional model with SMB forcing from years 1989 to 2010 (a 22 year simulation). During this period of time, we perform sensitivity and sampling analyses. Six flux gates are positioned throughout the NEGIS domain (see Figure 1b): one across each of the major outlets 79North (Gate N), Zachariæ Isstrøm (Gate Z), and Storstrømmen (Gate S); one across the northern branch of the NEGIS (Gate NB); and two across the main branch, one downstream (Gate MD) and one upstream (Gate MU). All mass fluxes responses are determined at the completion of the 22 year transient runs [*Schlegel et al.*, 2013; *Larour et al.*, 2012b].

We launch the transient UQ runs on the Amazon Elastic Compute Cloud (Amazon EC2), on 30 cpus for approximately 100 h, and the NASA Advanced Supercomputing Pleiades cluster, on 60 cpus for approximately 80 h. The model time step is 1.5 days, which satisfies the Courant-Friedrichs-Lewy condition.

4. Results

4.1. Sampling Analysis

Using sampling analysis, we quantify the mass flux uncertainty at predefined gates, as propagated through a forward model in response to random errors in model inputs. For each field, mass flux is calculated through the six flux gates noted as white lines in Figure 1b. As in *Schlegel et al.* [2013], we define uncertainty as the total range of each statistical distribution. The distribution plots represent the range and frequency of mass flux at the end of 500 independent random transient samples. A verification test of the sampling capabilities at the NEGIS outlet gates [after *Larour et al.*, 2012b] confirms that 500 samples are adequate for defining a significant uncertainty distribution of mass flux. We find that after 500 samples are completed, the standard deviation of mass flux converges, and above 500 samples it changes by only 1% per 100 additional samples.

In Figure 4, we present the statistical distributions of mass flux uncertainty resulting from errors in α, B_g, and B_r. We include mass flux uncertainty distributions for SMB for comparison. Table 1 summarizes sampling statistics for every field at each gate, including the mean, standard deviation, total value range, and the minimum and maximum 95% percentile of sample mass flux values. As an example of how extreme errors in fields may compound, we also include Figure 5. These results represent individual and combined sampling of B_r, extreme 150% α, and SMB at Gate NB.

All resulting distributions have little skew (skewness ranges from −0.10 to 0.25) with the exception of Gate NB SMB, which has a positive skew of 0.51. The general lack of skew indicates that SSA responds linearly and is well behaved in response to the imposed errors. This is especially true for B_g and B_r sampling (Figure 4, red/black), since the sampling distributions are forced uniformly, yet the responses are normally distributed (little skew).

Overall, we find that B_g is associated with the lowest uncertainties, while B_r is associated with larger uncertainties. However, we find that the small mass flux uncertainties due to B_g are not insignificant. For all gates except Gate MD, uncertainties are at least 500% larger than the annual internal mass flux variability of the flux gates over the 22 year sampling period, and for Gate MD, the uncertainties are 240% larger than the model interval mass flux variability. For B_r, the outlet glaciers (i.e., Gates N and Z) account for ice flux uncertainty of over 12% and 13%, respectively, about 4 times larger than B_g, and comparable to the uncertainty

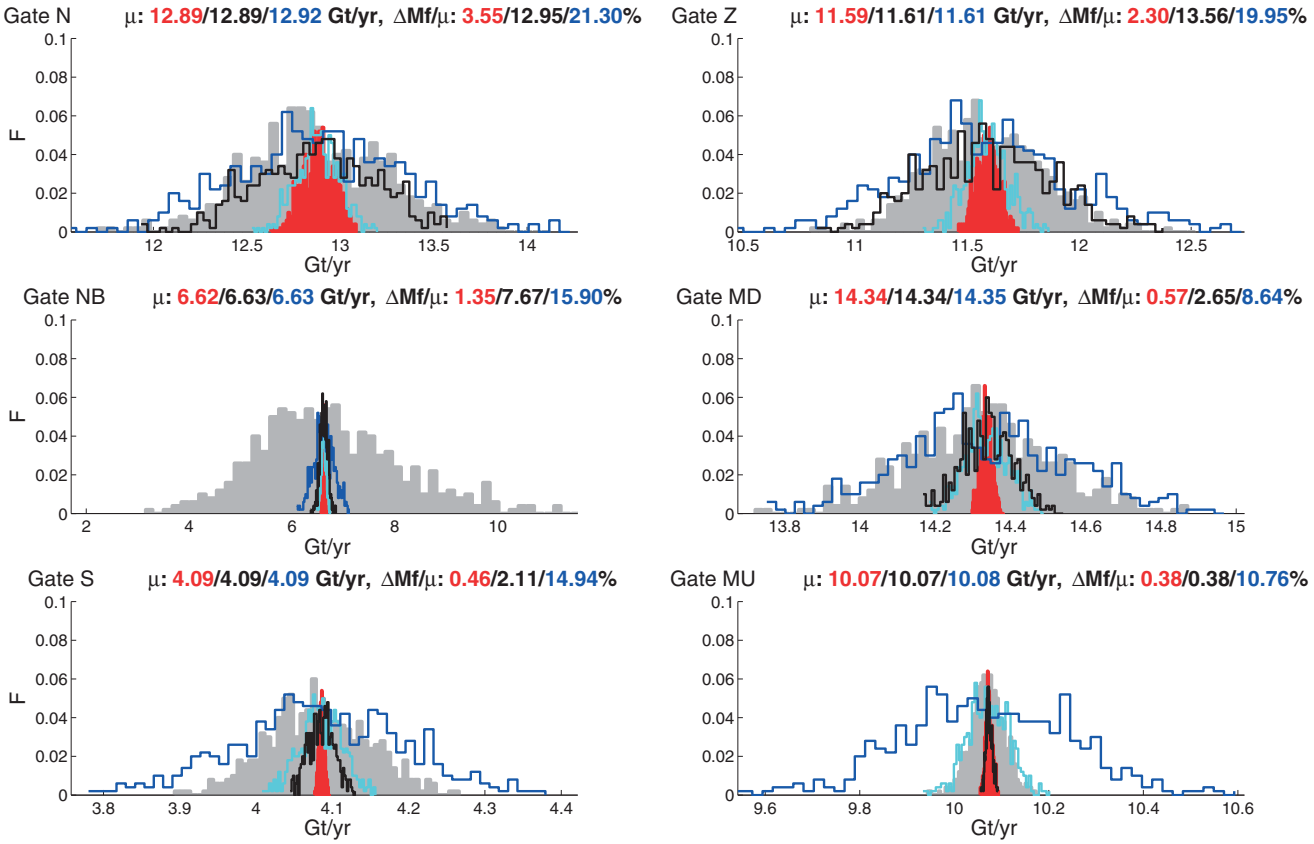

Figure 4. Histograms for sampling studies of B_g (due to error in geothermal heat flux = red), B_r (due to geothermal heat flux in the accumulation area and CH refreeze in the ablation area = black), and α (with constant $3e_\alpha$ of 5% = cyan and 20% = blue), including frequencies (F) of mass flux (Mf) across the six gates specified in Figure 1b. Results of SMB sampling (gray) are also included for comparison [*Schlegel et al.*, 2013]. We sample a 22 year run 500 times. All runs are forced with the same base SMB time series 1988–2010. For each sample, fields are perturbed spatially by random values falling within a distribution with standard deviation equal to e (For error values, see Figure 3b for B_g and Figure 3d for SMB.). For B_r, the error distribution is represented by a range of 42% the value of B [*Phillips et al.*, 2010]. For α, $3e$ is 5% and 20%. We provide, for B_g, B_r, and 20% α, output means (μ) and percent uncertainty, defined as the total range of the distribution (Δ) relative to μ (in %). Associated statistics for all fields are summarized in Table 1.

due to SMB. For these main outlet glaciers, B_r uncertainty is, respectively, comparable to a 25% (not shown) and a 20% change in α, while uncertainty in B_g is comparable to about a 5% change in α. For all upstream gates, uncertainty in B_g is 1% or less, comparable to a 1–2% change in α (not shown). For Gates NB, MD, and S, which are located tens of kilometers upstream of ablation area, the uncertainties due to B_r are larger than B_g and comparable to about a 5% change in α. Since B_g is only imposed in the ablation area, these results indicate that errors imposed tens of kilometers downstream from the gates are responsible for uncertainties in mass flux at Gates NB, MD, and S. Gate MU, however, which is hundreds of kilometers upstream from the ablation area, is not affected by the imposition of B_r errors in the ablation area, as uncertainties due to B_g and B_r are equivalent (Table 1).

These results indicate that the areas of fast flow near the outlets are more susceptible to errors than are the upstream areas. Indeed, with exception of the SMB uncertainty at Gate NB, it is 79North and Zachariæ Isstrøm outlets (Gates N and Z) that are the most uncertain due to errors in B_g, B_r, α, and SMB. For B_g, B_r, and SMB, the mass flux uncertainties become smaller 50–100 km upstream of the outlets (Gates S, MD, and NB for B_g and B_r), while the smallest uncertainties are found 300 km upstream of the outlets (Gate MU). This is also the case for α, with the exception of Gate MD (which has the lowest uncertainty and is associated with an isolated "hole" of very low sensitivity; see section 4.2 and Figure 7, Gate MD). Note that in the majority of the ice stream, SSA is a reasonable choice for simulating the high-velocity ice flow, particularly the downstream gates, where our results indicate uncertainties that are the most significant. Therefore, our confidence in these results is high, especially for Gates NB, MD, and S. For Gates N and Z, which correspond to narrow outlet areas of fast flow and high basal slip (Figures 2c and 2d), we have reasonable confidence in

Table 1. Statistics for Sampling Histograms in Figure 4[a]

Variable	B_g	B_r	Fc 5%	Fc 20%	SMB
		Gate N			
μ	12.89	12.89	12.89	12.92	12.90
95% Min	12.75	12.39	12.70	12.18	12.31
95% Max	13.02	13.37	13.08	13.68	13.53
σ	0.083	0.31	0.11	0.45	0.38
ΔMf	0.46	1.67	0.68	2.75	2.43
ΔMf/μ (%)	3.55	12.95	5.30	21.30	18.82
		Gate Z			
μ	11.59	11.61	11.59	11.61	11.60
95% Min	11.52	11.16	11.45	11.01	11.21
95% Max	11.67	12.06	11.75	12.25	12.02
σ	0.050	0.28	0.094	0.38	0.25
ΔMf	0.27	1.57	0.57	2.32	1.72
ΔMf/μ (%)	2.30	13.56	4.94	19.95	14.80
		Gate NB			
μ	6.62	6.63	6.63	6.63	6.83
95% Min	6.60	6.51	6.54	6.32	4.77
95% Max	6.65	6.75	6.71	6.99	9.46
σ	0.014	0.077	0.050	0.20	1.41
ΔMf	0.090	0.51	0.27	1.05	8.63
ΔMf/μ (%)	1.35	7.67	4.02	15.90	126.36
		Gate MD			
μ	14.34	14.34	14.34	14.35	14.33
95% Min	14.31	14.23	14.25	13.98	14.02
95% Max	14.36	14.45	14.43	14.71	14.66
σ	0.015	0.069	0.056	0.22	0.19
ΔMf	0.082	0.38	0.31	1.24	1.15
ΔMf/μ (%)	0.57	2.65	2.16	8.64	8.05
		Gate S			
μ	4.09	4.09	4.09	4.09	4.09
95% Min	4.08	4.06	4.04	3.91	3.98
95% Max	4.09	4.12	4.13	4.27	4.20
σ	0.0032	0.017	0.028	0.11	0.067
ΔMf	0.019	0.086	0.15	0.61	0.37
ΔMf/μ (%)	0.46	2.11	3.71	14.94	9.17
		Gate MU			
μ	10.07	10.07	10.07	10.08	10.07
95% Min	10.06	10.06	10.01	9.80	10.01
95% Max	10.09	10.09	10.14	10.37	10.13
σ	0.0070	0.0070	0.045	0.18	0.035
ΔMf	0.038	0.038	0.27	1.08	0.24
ΔMf/μ (%)	0.38	0.38	2.71	10.76	2.33
		NEGIS Outflux			
Gates N + Z + S					
μ	28.57	28.59	28.57	28.61	28.59
ΔMf	0.74	3.33	1.41	5.68	4.52
ΔMf/μ (%)	2.60	11.65	4.93	19.84	15.81

[a]Statistics include the following: mean mass flux (μ in Gt/yr), the minimum and maximum mass flux values for the 95 percentile of samples (Gt/yr), the standard deviation of the sampling distribution (σ in Gt/yr), the total range of mass flux values (ΔMf in Gt/yr), and the percent mass flux uncertainty (defined as ΔMf/μ in percent).

the results. We are least confident about the uncertainties in mass flux at Gate MU, which is associated with the smallest uncertainties. This is because Gate MU is located upstream where mesh resolution is low, basal drag becomes larger, and SSA begins to break down.

Gate NB SMB results stand out as extreme amongst the distribution responses. At this gate, mass flux responds dramatically to SMB errors and uncertainties range by over 125%. This uncertainty range is comparable to a 150% change in the basal drag coefficient (Figure 5). In an area 30 km upstream of Gate NB, we find average SMB values that are small and positive, while e_{SMB} is greater than 0.3 m/yr water equivalent, resulting in large percentage perturbation (P_i) values. For the sampling analysis, large positive P_i values in this area upstream are responsible for a 76% increases in mass flux through Gate NB, and large negative P_i values are responsible for a 56% decrease in mass flux. As a result, the Gate NB distribution has a slightly positive skew (Figure 4). Since the SMB P_i distribution forcing is normally distributed, a skewed response indicates that the northern branch of the NEGIS (Gate NB) is dynamically responsive to changes in SMB. Specifically, we find that in agreement with *Schlegel et al.* [2013], more upstream accumulation drives an increase in ice flow, and less upstream accumulation impedes flow. Note that the response cannot be explained by advection only, since the ice velocity upstream is about 500 m/yr and the local changes in ice thickness could not advect as far as 30 km during the 22 year sampling period.

As an example of extreme sampling, we also include results of combined error sampling (Figure 5). Here we focus on Gate NB, since it was the gate affected by a large percent uncertainty in SMB. For this example, B_r and SMB errors are combined with a 150% error margin in basal drag coefficient. Individually, B_r, 150% change in α, and SMB, respectively, result in approximately

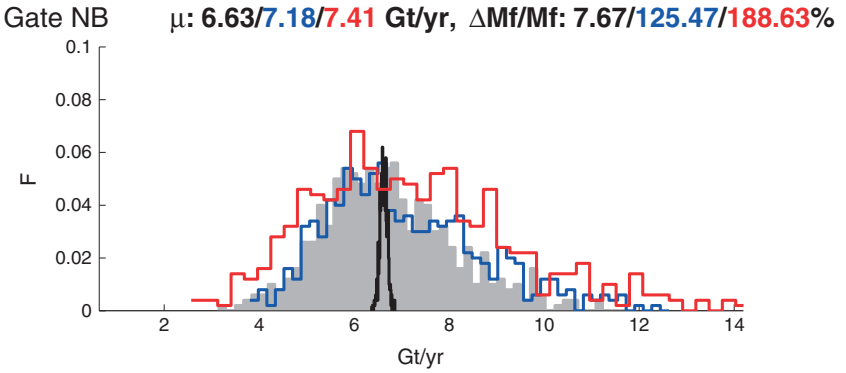

Figure 5. Histograms for sampling studies of the combination of B_r, α ($e_\alpha = 150\%$), and SMB errors (red); α with constant $e_\alpha = 150\%$ (blue); B_r (black); and SMB (gray) [*Schlegel et al.*, 2013]. Histograms represent the frequencies (F) of mass flux (Mf) across Gate NB (Figure 1b). All errors defined as for Figure 4. Mass flux means (μ) and percent uncertainty, defined as total range of the distribution (Δ) relative to μ (in percent), are provided for B_r, 150% α, and combined sampling. Histogram results represent the mass flux at the end of 500 individual 22 year runs forced with the same base SMB time series (1988–2010).

7%, 125%, and 126% uncertainty in Gate NB mass flux. Combined, we find that they contribute to 188% uncertainty, which is equivalent to a 6σ mass flux uncertainty of about 13.6 Gt/yr for the northern branch of the NEGIS.

4.2. Sensitivity Analysis

In Figures 6–8 we plot B and α sensitivity results for our six flux gates. These sensitivities represent the magnitude of mass flux change (Gt/yr) at each gate in response to a 0.1% perturbation in B and α in other parts of the domain. The coloring of a particular partition indicates how a perturbation within that partition will change the mass flux through the gate marked in white. Sensitivities for SMB at Gates N, NB, and S are also presented, for comparison, to illustrate how mass flux sensitivities to B and α differ from the sensitivities to SMB (Figure 9). We include these gates because they were not presented in *Schlegel et al.* [2013]. Note that the perturbation in each field is a percent value, so quantitative comparison of sensitivities between the fields has little meaning. However, if we compare the magnitudes of the sensitivities, it is clear that small changes to α affect mass flux more significantly than do changes to B (Figures 6–8). It is also clear that mass flux is least sensitive to changes in SMB (Figure 9).

Sensitivity coloring indicates whether a positive perturbation at a particular location is directly (red) or inversely (blue) related to mass flux. For example, in Figure 6, the sensitivities for Gates N and Z are overwhelmingly blue. These results suggest that at the outlet gates, mass flux is inversely related to perturbations in B and α at the locations shaded in blue. This general relationship also holds for the other gates (Figures 7 and 8), though the spatial patterns vary widely for each gate. Overall, the blue shading illustrates that an increases in the ice viscosity parameter or in the basal drag coefficient, either upstream or downstream of a gate, will decrease mass flux through that gate. Note that we also find red-shaded areas lateral to the gates (e.g., Figure 7), indicating the opposite effect that an increase in either field at these locations will result in mass flux increase at the gate. These results suggest that when lateral flow is slowed down by increases in the ice viscosity parameter or the basal drag coefficient, less ice is advected downstream, and as a result, ice accumulates upstream. This effect increases the local surface slope, and the ice flow becomes more concentrated at the flux gate. As a result, we see an increase in mass flux through the gate.

Though clear similarities exist between the mass flux sensitivities for B and α, their spatial patterns differ distinctly. For instance, we find that the B sensitivities have spatial "holes" that are located just downstream of all gates, most strikingly at Gates NB, MD, S, and MU (Figures 7 and 8). It is important to note that the location of these features correspond to large cross-flow gradients in B. Gate MU, for example, cuts across a strong B gradient at the location marked P5 (Figure 3a). We find that when a sharp gradient in B occurs within a specific partition, then the (0.1%) perturbation of B is asymmetric. As a result, the flow in the area with the greater B value slows down. Ice is diverted toward the part of the partition with a lesser B value, and the ice within this section speeds up. The speedup counteracts the expected slowdown due to an increase in the ice viscosity parameter, and as a result, the overall mass flux through the gate does not change.

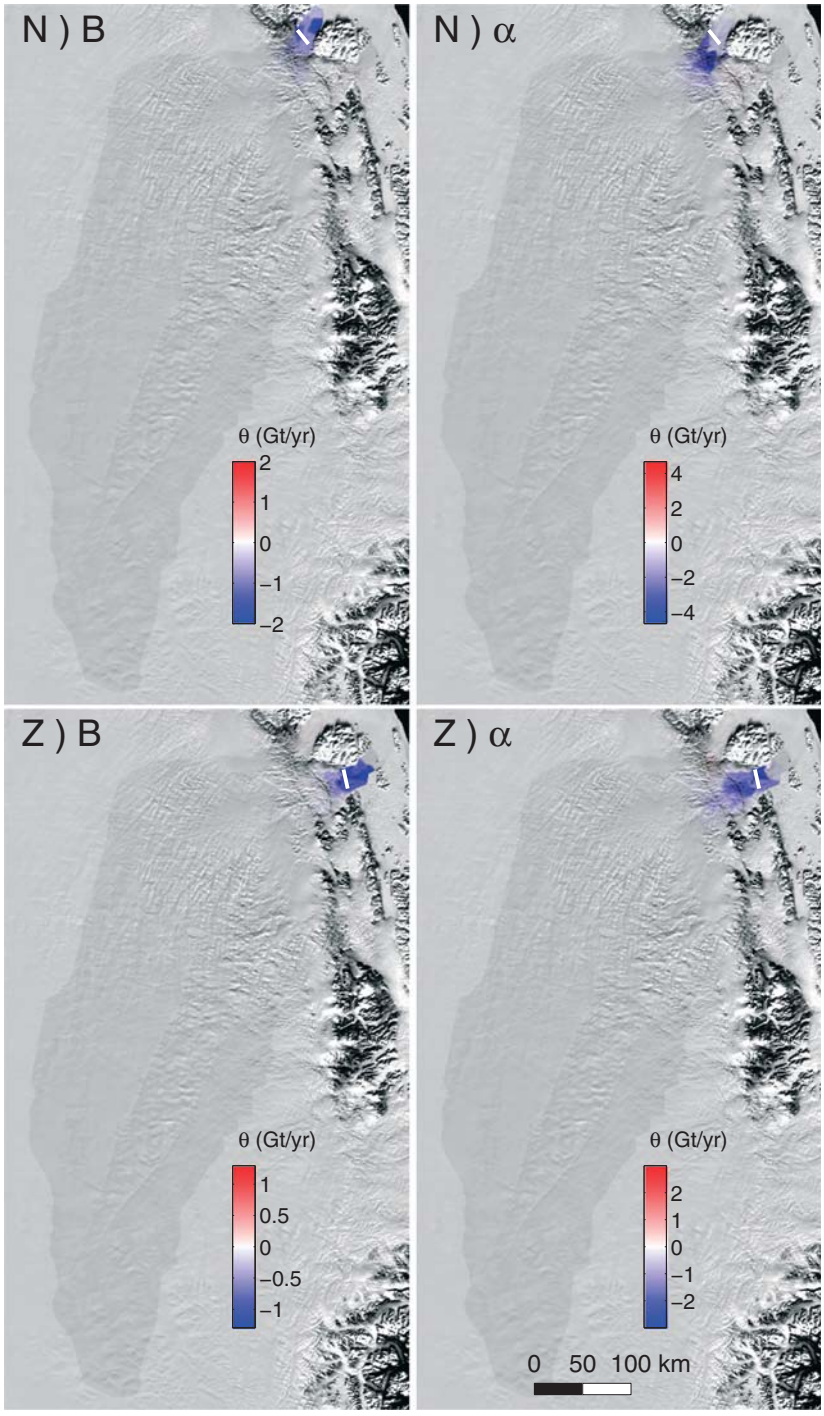

Figure 6. Sensitivity (θ, Gt/yr) of Gates N and Z (Figure 1b) relative to error in B and α. The domain is partitioned into 1000 regions. The variable value in each partition is perturbed by 0.1% and used as forcing for a distinct model run. Sensitivities (output:input) assess the impact of errors on the mass flux through each gate.

Similar examples can be seen downstream of Gates NB, MD, and S (Figures 7 and 8). As observed for Gate MU, downstream of these gates, we find high-velocity flow and a relatively strong cross-flow gradient in B (Figure 3a, P2–P4).

The sensitivities for α reveal a similar "hole" just downstream of Gate MD (Figure 7), where we find a large region of near-zero sensitivities. Results suggest that this feature is associated with an area of high-velocity flow and a very low basal drag coefficient (Figures 2c and 2d, P1). In fact, the inferred values of α are so low

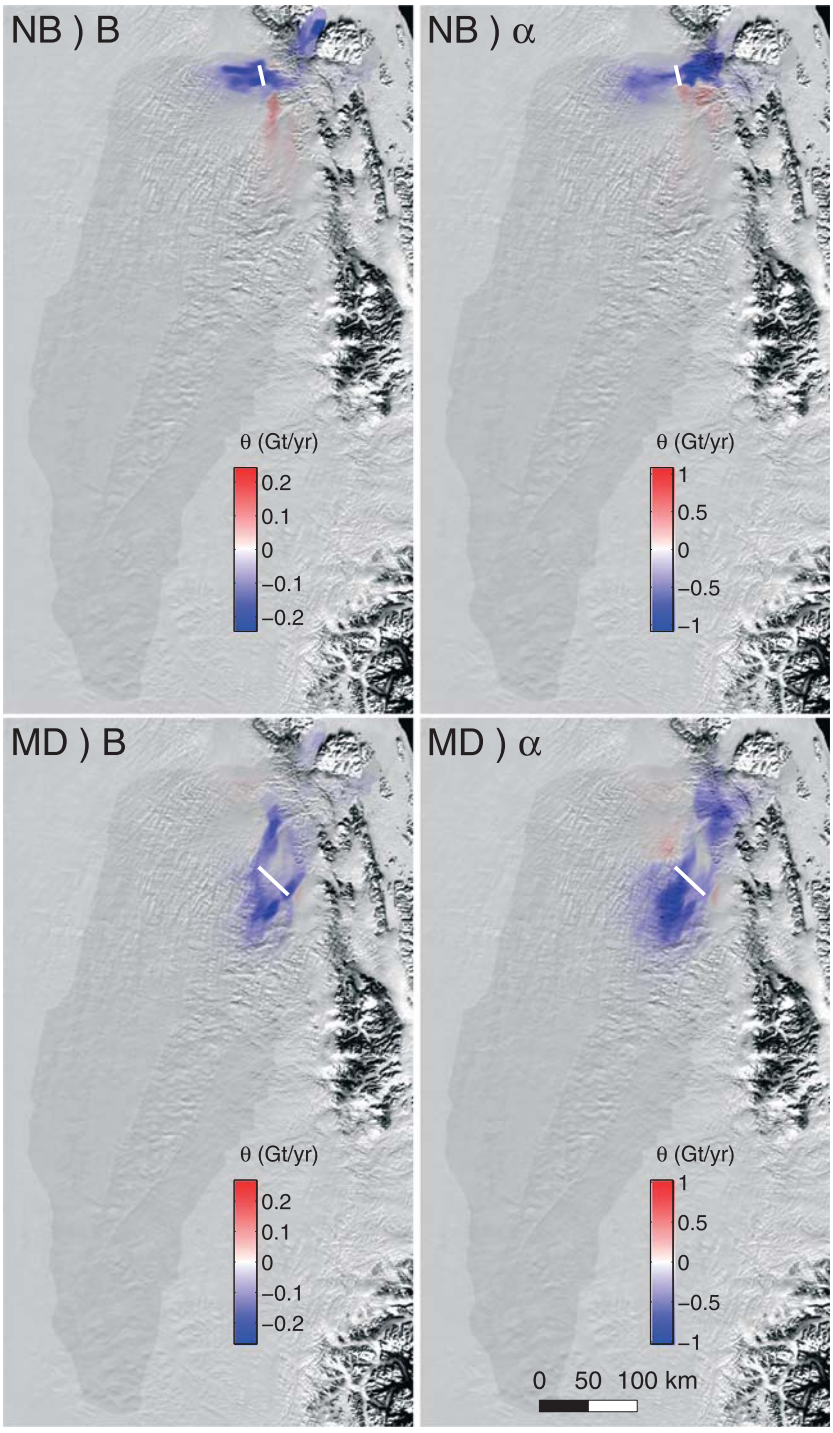

Figure 7. Sensitivity (θ, Gt/yr) of Gates NB and MD (Figure 1b) relative to error in B and α. The domain is partitioned into 1000 regions. The variable value in each partition is perturbed by 0.1% and used as forcing for a distinct model run. Sensitivities (output:input) assess the impact of errors on the mass flux through each gate.

in this region that small perturbations have very little effect on the mass flux gates upstream. This sensitivity hole is highlighted distinctly by all scaled sensitivities plots for α (i.e., Figures 10–12).

While perturbations in B and α decrease mass flux both upstream and downstream of all gates, we find that this differs significantly from how SMB affects flow (Figure 9). Specifically, an increase in SMB upstream from the gate increases mass flux, while an increase downstream decreases the flux. In agreement with *Schlegel*

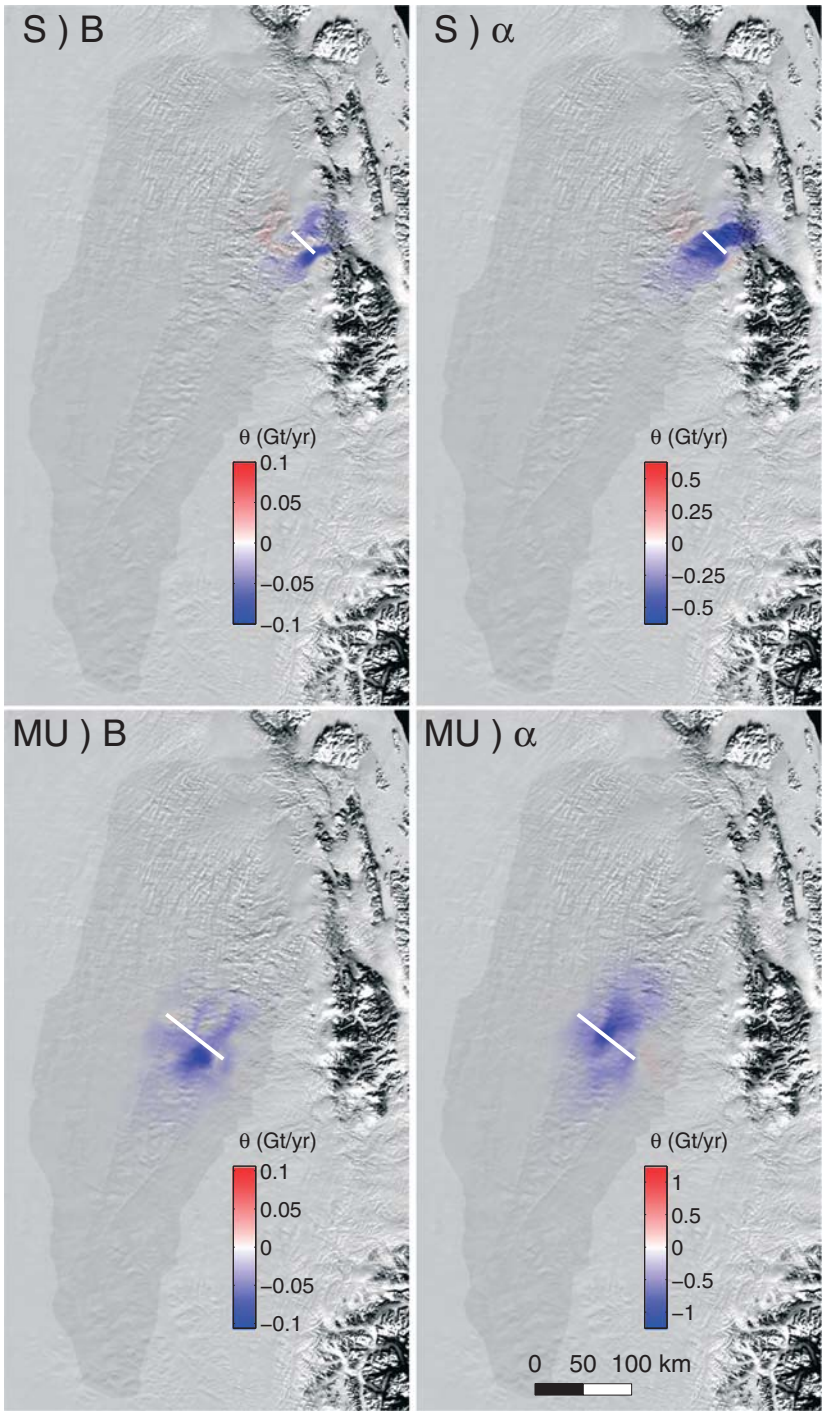

Figure 8. Sensitivity (θ, Gt/yr) of Gates S and MU (Figure 1b) relative to error in B and α. The domain is partitioned into 1000 regions. The variable value in each partition is perturbed by 0.1% and used as forcing for a distinct model run. Sensitivities (output:input) assess the impact of errors on the mass flux through each gate.

et al. [2013], these results indicate that changes in SMB modify the local flow by altering the surface slope and driving stress. Note that the SMB results exhibit opposite sensitivities for partitions in the ablation area (e.g., Gates N and NB), where SMB and the SMB perturbations are negative (Figure 3a).

The sensitivity results presented here also give us information about the spatial extent of changes to B and α. For example, we find that Gate NB, which runs across the northern branch of the NEGIS, increases in mass flux when there is an increase in B or α in the main trunk of the ice stream. This is indicated by the red

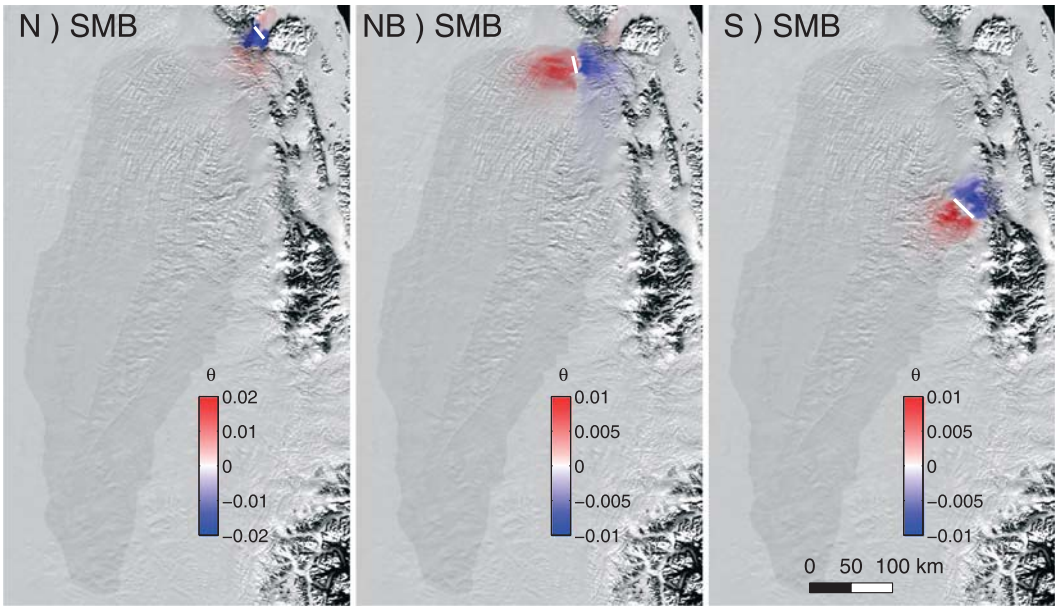

Figure 9. Sensitivity (θ, Gt/yr) of Gates N, NB, and S (Figure 1b) relative to error in SMB after *Schlegel et al.* [2013]. The domain is partitioned into 1000 regions. The variable value in each partition is perturbed by 0.1% and used as forcing for a distinct model run.

coloring in the main trunk in Figure 7, Gate NB. This effect is also visible for Gate MD, which spans the main trunk (Figure 7). In these plots, small positive (light red) sensitivities are found in the northern branch of the ice stream, indicating that positive changes to B and α in the vicinity of Gate NB can positively affect mass flux through Gate MD.

Scaled sensitivity (SS) plots help emphasize this interconnection between flow in main trunk and within the ice stream branches. In Figures 10–12, we plot the corresponding SS (dimensionless) for B and α. SS are plotted on a logarithmic scale and are used to compare the spatial extent of influence of different fields. For all gates, it is evident that the sensitivities have a large extent and that perturbations in ice flow propagate along the high-velocity flow lines of the ice stream, where SSA is most valid. In Table 2, we quantify the spatial extents for each gate. The table summarizes (for each field at every gate) the radius of influence for various orders of magnitude of scaled sensitivities (as defined in section 2.2). For comparison, we present SMB SS results in Figure 13 and include the mean SMB radii of influence for all gates in Table 2.

Results for all gates and fields suggest that though mass flux is most sensitive to local changes, it can also be affected by very small changes that occur over 250 km away. The average first-order radius of influence for α is 40 km, which is comparable to that of SMB (Table 2). For B, the first-order radius of influence is 61 km. In particular, it is the Gates NB and MD which have first-order radii of influence of 92 and 80 km, respectively, and bias the mean for B. Figure 11 indicates that the first-order extents of Gates NB and MD reach to the merge between the main branch and the northern branch, and the second-order extents reach as far as the margins of 79North and Zachariæ Isstrøm (Figure 11, B, pink). Because increases (decreases) in B will lead to an overall stiffening (softening) and a thickening (thinning) of local ice, sensitivities for B include the propagation of a local change to both velocity and thickness. Changes to α, on the other hand, affect only local velocities to first order. These results suggest that changing B at a dynamic outlet glacier margin could propagate 100 km upstream and affect the upstream mass flux to first order.

On average, B and α have an overall larger extent of influence than does SMB. And although Table 2 indicates that the average extent for gates are similar in value, SS results in Figures 10–12 suggest that they vary spatially and are largely dependent on the original spatial distribution of the field's values. Since B and α are constant through time, this effect is more striking. On the other hand, SMB is a transient forcing. Therefore, we find that the SMB SS patterns are more diffuse and do not exhibit the patchwork appearance associated with the constant fields.

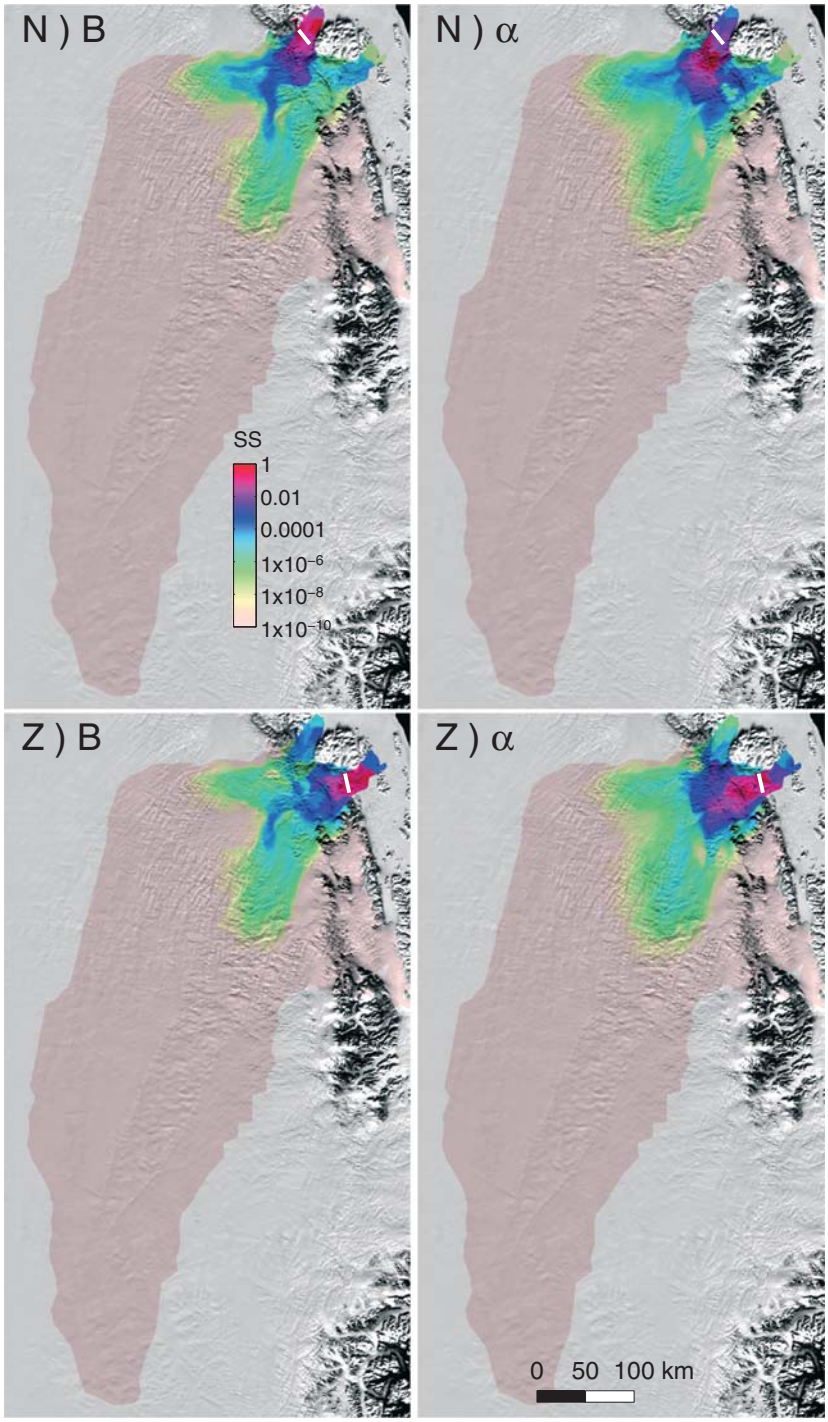

Figure 10. Scaled sensitivities (SS, unitless) of Gates N and Z (Figure 1b), calculated by scaling the square of the sensitivity values plotted in Figure 6. Scaled sensitivities sum to unity over the domain. Results are displayed on a logarithmic scale in order to emphasize the extent of the local influence of error on each flux gate.

5. Discussion

Results illustrate that changes to the ice viscosity parameter and the basal drag coefficient affect local ice flow, as well as nonlocal flow. For B and α, a decrease in these fields directly enhances local ice velocity. Additionally, the spatial patterns of the initial B and α fields, especially local patterns, play an important role in dictating how ice flow responds. These results differ from SMB sensitivity results, which suggest that mass

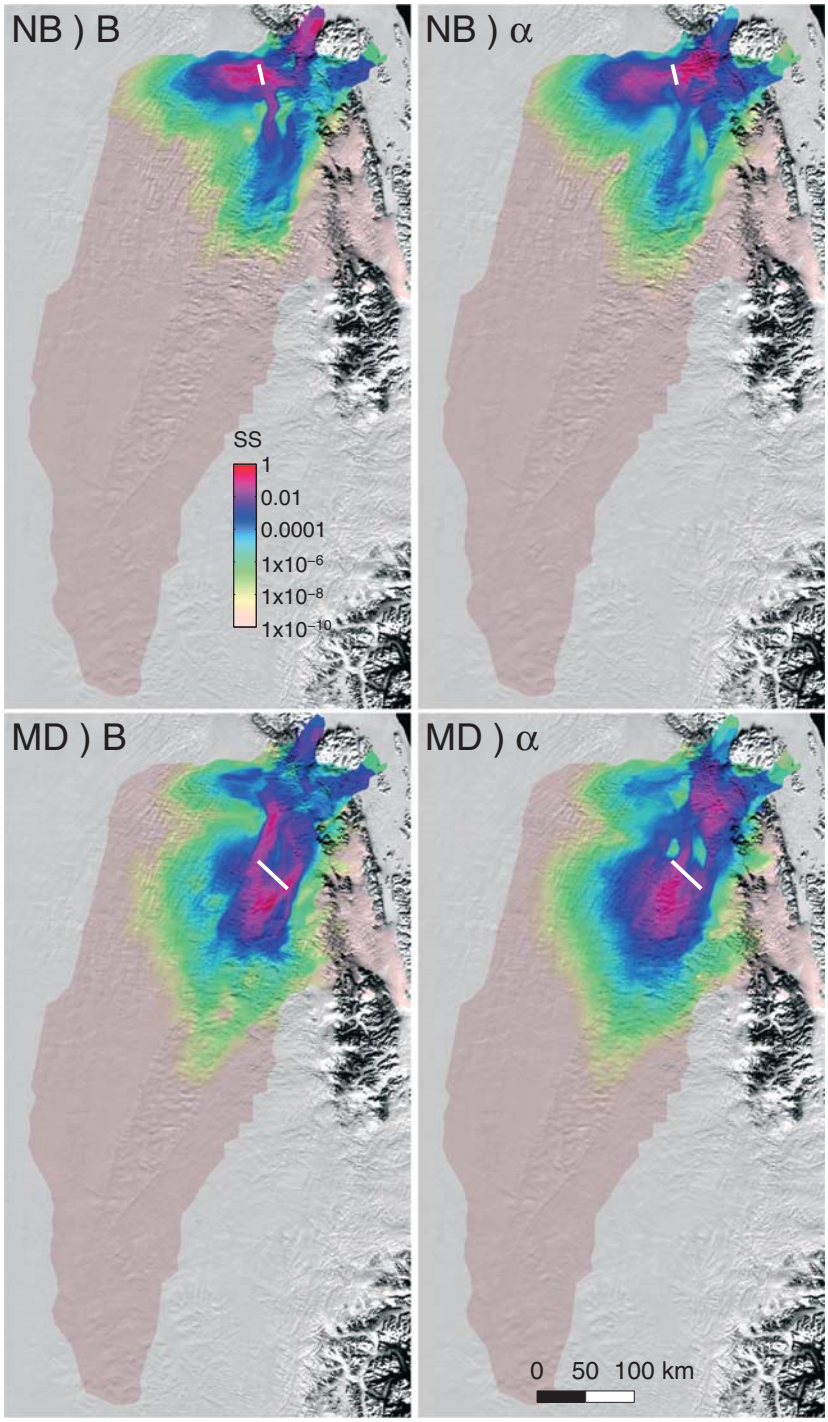

Figure 11. Scaled sensitivity (SS, unitless) of Gates NB and MD (Figure 1b), calculated by scaling the square of the sensitivity values plotted in Figure 7. Scaled sensitivities sum to unity over the domain. Results are displayed on a logarithmic scale in order to emphasize the extent of the local influence of error on each flux gate.

flux is strongly affected by the spatial gradient of the change in SMB forcing. Overall, we find that in order to accurately simulate the ice flow regime of a specific domain, the spatial variability of B, α, and SMB must be correctly captured. We also find that local perturbations in ice flow, due to perturbations in any of these fields, can cause secondary effects that alter the ice flow upstream and downstream, far from the original perturbation, suggesting that they must be well represented throughout the domain. To a greater extent than SMB, such a change in B or α is capable of altering distant flow up to 300 km away after a period of

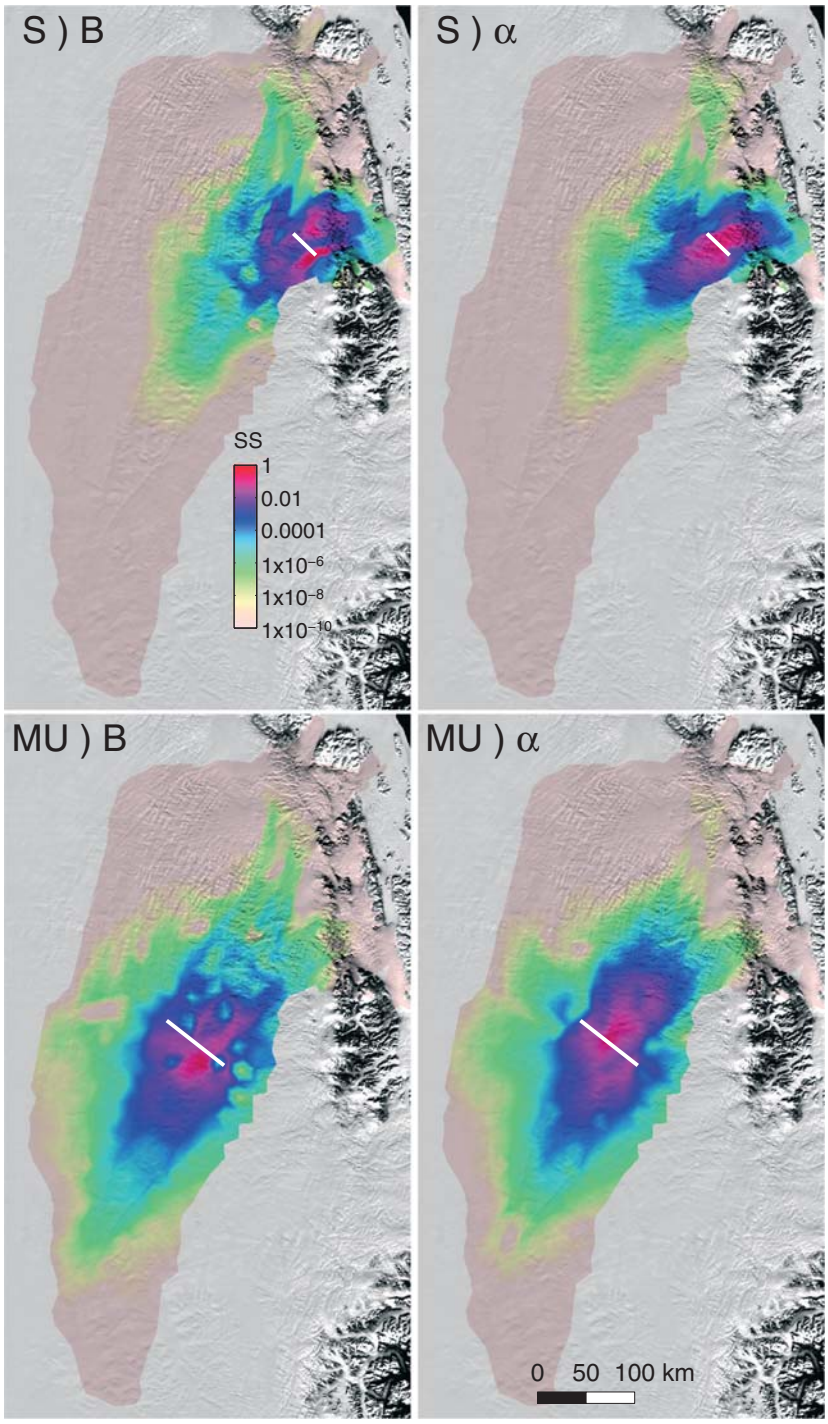

Figure 12. Scaled sensitivities (SS, unitless) of Gates S and MU (Figure 1b), calculated by scaling the square of the sensitivity values plotted in Figure 8. Scaled sensitivities sum to unity over the domain. Results are displayed on a logarithmic scale in order to emphasize the local influence of error on each flux gate.

only 22 years (Table 2 and Figures 10–12). Additionally, it is clear that small changes to α and B can affect the flow in other branches of the ice stream. For example, an increase in either of these fields within the NEGIS main branch causes the main branch to slow (Figure 7, Gate MD), and as a result, less ice is advected toward the outlets. In response, the northern branch speeds up to compensate for the deficit (Figure 7, Gate NB). These results extend our earlier findings [*Schlegel et al.*, 2013] (which specifically focused on the

Table 2. The Maximum Radius of Influence (km) of B and α Errors on Ice Flux Through Six Gates, as Measured by Scaled Sensitivities (Figures 10–12)[a]

Order of Magnitude	−1	−2	−3	−5	−10
		B			
N	31.4	41.8	57.2	136.3	235.0
Z	33.5	33.5	45.0	123.5	219.6
NB	91.8	91.8	119.3	161.4	237.1
MD	80.3	93.7	178.0	187.3	253.1
S	40.2	58.8	76.3	132.8	270.4
MU	60.7	82.7	118.3	190.5	321.0
Mean	61.3	72.1	107.4	159.1	260.2
		α			
N	41.6	57.2	68.6	136.3	260.7
Z	36.0	63.5	73.4	140.4	246.7
NB	45.6	60.5	76.6	161.4	251.7
MD	37.1	54.3	135.9	173.0	274.3
S	33.9	112.1	77.7	122.2	279.3
MU	41.7	82.7	105.2	175.5	310.5
Mean	40.2	76.6	93.8	154.5	272.5
		SMB			
Mean	39.1	63.7	82.9	153.1	253.9

[a]For comparison, we also included the mean SMB radius of influence for each gate. Values are given for multiple orders of magnitude of scaled sensitivities (log10, ranging from 10^{-1} to 10^{-10}). For all variables, small influences can be found as far as 250 km from the flux gate. Errors due to α have an average first-order radius of influence around 40 km radius, which is comparable to that of SMB. In contrast, B errors have a larger first-order radius of influence, with an average of 61 km. The radius of influence for B is similar to α and SMB in the outlets but largest upstream. In general, α and B errors have more extensive influences on mass flux than do SMB errors, but relative influence of each variable is unique depending on the gate and regional characteristics of ice flow.

effects of SMB errors on mass flux in the main branch and at the Zachariæ Isstrøm outlet) to the entire NEGIS basin. Here we further exemplify that the ice stream can dynamically accommodate for shifts in neighboring flow, particularly in areas of high velocity. Consequently, we find that ice flow throughout the ice stream is interconnected, and the NEGIS is an ideal example of these dynamics.

This is especially the case for changes to ice flow resulting from perturbations in the ice viscosity parameter. The first-order radii for B (Table 2) and the scaled sensitivity results for the upstream gates (Figure 7, Gates NB and MD, and Figure 8, Gate MU) suggest that for a dynamic, fast-flowing regime, changes to flow within tens of kilometers from a flux gate can influence mass flux just as strongly as local changes. For α, the results are similar, though they do not exemplify the effect as well. Most likely this is because B affects both the local flow properties of the ice as well as the local thickness, especially at the margins where ice flow is not constrained by downstream ice due to ISSM's free-flux condition at the margins [*Larour et al.*, 2012c]. As a result, changes to B result in the upstream propagation of changes to local ice velocity and thickness (i.e., Figure 7). Overall, B sensitivities best illustrate the extensive spatial influence that small perturbations have on nonlocal dynamics, particularly in the fastest-flowing areas of the ice stream.

While sensitivity results suggest that flow is strongly connected within a flow line, they also provide evidence for a correlation between lateral flow. First, for B and α (in contrast to the negative sensitivities in most of the NEGIS domain), lateral ice flow has a positive sensitivity (i.e., Figure 7, Gate MD, and Figure 8, Gate MU). This suggests that local ice flow accelerates in response to a lateral increase in B or α, as mass flux through the gate increases in order to compensate for ice not being advected laterally. Sensitivity results also suggest that ice flow will divert due to perturbations in B. The most striking exemplification of this is found upstream in the main branch of the NEGIS (i.e., Figure 8, Gate MU). Just downstream of the most upstream gate, in contrast with the negative sensitivities dominating the rest of the domain, there is an isolated partition with a sensitivity of nearly zero. Here the spatial characteristics of B, specifically strong cross-flow gradients (Figure 3a, P2–P5), divert flow through the gate and lead to little change in mass flux. Such connections between lateral flow indicate that when forced with changes to neighboring ice properties, ice flow is capable of dynamically compensating by deviating and altering its mass flux spatially. As a consequence, we find that spatial variability in these fields affects the simulation of ice flow, and their transient evolution should be taken into account in the forward modeling of a dynamic ice regime. Specifically, it is important for models to consider how ice characteristics may change as basal hydrology and thermal conditions evolve in response to the introduction of meltwater runoff into the subglacial system. Furthermore, results suggest that flow line models, which consider only changes upstream and downstream of a particular location, would not sufficiently simulate the dynamic behavior of an ice stream. Thus, in order to accurately capture

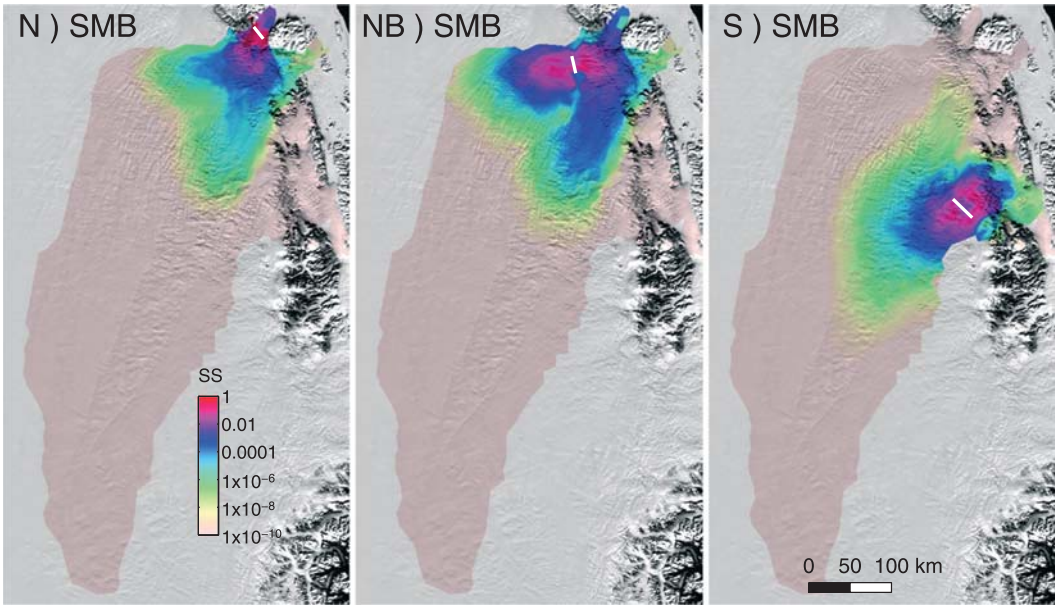

Figure 13. Scaled sensitivity (SS, unitless) of Gates N, NB, and S (Figure 1b), calculated by scaling the square of the SMB sensitivity values plotted in Figure 9. Scaled sensitivities sum to unity over the domain. Results are displayed on a logarithmic scale in order to emphasize the extent of the local influence of error on each flux gate.

ice stream response to transient perturbations in forcing, it is necessary to use a plan view model. Similarly, we find that in order to capture all the details of ice flow and accurately simulate this dynamic feature of the Greenland Ice Sheet, it is important to use high-resolution spatial maps of boundary conditions and forcing, particularly within the narrow outlet glaciers, where flow is the most uncertain (Figure 4). Indeed, the radii of influence presented in Table 2 suggest that like SMB, α should be known at a resolution of at least 40 km and B of at least 60 km, in order to accurately capture the ice flow regime. As discussed by *Schlegel et al.* [2013], this is especially true considering that small changes in field values propagate along the flow, hundreds of kilometers upstream and downstream. The case is even stronger for B and α because such changes are strongly linked to perturbations in lateral flow.

Overall, sensitivity results suggest that flow is most sensitive to changes in α, especially far upstream, where errors in B and SMB are less critical (Figures 6–8). These results also suggest that mass flux is more sensitive to B than it is to SMB. However, when we compare the uncertainties resulting from errors in SMB with errors in B due to geothermal heat flux or CH refreeze, we find that (in agreement with *Seroussi et al.* [2013]) SMB is actually responsible for more uncertainty. This is especially the case in locations where SMB is small and percent errors are large (i.e., the equilibrium line or Gate NB). In these locations, errors in SMB can be significant and are capable of driving sizable, and possibly nonlinear, changes in mass flux on decadal time scales, even when relative sensitivities indicate that flow is less sensitive to small changes in SMB than to small changes in the ice viscosity parameter or the basal drag coefficient. Indeed, mass flux uncertainties due to B_g errors range from less than 1% upstream to almost 4% at the northern outlets, while B_r errors result in uncertainties ranging from less than 1% upstream to 13% at the northern outlets. In comparison, SMB errors range from 2% upstream to 15% and 19% at the northern outlets to an extreme value of 126% in the northern branch of the NEGIS (Table 1). The extreme value of mass flux uncertainty in the Northern branch of the ice stream illustrates how spatial shifts in climate can impact the ice flow regime on decadal time scales.

In general, uncertainties in B_g are comparable to less than a 5% error in α. This suggests that since ISSM uses inversion to calculate α with consideration to a constant B field (after a thermal steady state is established), error due to geothermal heat flux is not likely to affect results of a decadal-scale forward model. We find that α and B affect ice flow similarly, and an inversion using a different B would produce α values that directly compensate for the modified geothermal heat flux input. Indeed, our result suggest that use of a different geothermal heat flux would alter α values by up to 5%, resulting in little difference between the two post-spinup estimates of NEGIS ice flow. In contrast, estimated errors in B_r affect flow in a much more significant way, especially in the outlet glaciers. Here uncertainties in mass flux are equivalent to the uncertainties due

to SMB errors, suggesting that in an extreme warming scenario, ice heating due to CH refreeze may be large enough to increase marginal velocities and enhance ice discharge. As a result, we find that geothermal heat flux map has little effect on the outcome of decadal-scale ice flow simulation in this region. In contrast, it is the processes that may alter the spatial variation in B_r, α, and SMB, especially in proximity to the outlet glaciers that must be well represented in order to properly capture the NEGIS flow regime and its dynamic response to transient climate conditions.

These results have implications for climate warming scenarios, especially in the ablation area where runoff is likely to increase. Due to their low elevations and proximity to the ocean, the relatively fast-flowing outlets are the most susceptible to increased melt rates. Increases in melt would not only increase ice flow by changing SMB but may also lead to decreases in α (i.e., through basal hydrology) or B (i.e., through heating of ice due to CH refreeze). The compound influence of these factors may be significant, especially because these areas are both susceptible to climate change and associated with the largest uncertainties in mass flux (see section 4.1 and Figure 4). Indeed, we find that the α uncertainties for the outlet glaciers are nearly double those of the gates located farther upstream. It is also clear that B_r plays a much more significant role in lower elevations, as its uncertainty is equivalent to that of SMB in proximity to the outlets. If decreases in α or B did accompany warming along the ice sheet margins, sensitivity results suggest that this would lead to increases in outlet discharge and in mass flux hundreds of kilometers upstream. We find that NEGIS is a dynamically active feature and, in response to changes at the margin, is capable of advecting ice from the ice sheet interior. If NEGIS is dynamically efficient enough to maintain contact with the North Atlantic in a warmer climate, marginal warming could result in drawdown of ice from the ice sheet interior and thinning at Greenland's highest elevations. This behavior has important consequences for future mass balance projections of the Greenland Ice Sheet [*Khan et al.*, 2014], especially because uncertainties are largest in the ablation area. In a warming climate, the ablation area is expected to expand, and melt is expected to occur much more frequently at higher elevations, resulting in smaller SMB, more spatial influence of CH warming and basal sliding, and larger errors associated with these processes. Results indicate that upstream mass flux is responsive to these climate-driven changes on decadal time scales. Considering that large errors are already associated with the prediction of future climate, it is clear that ice sheet model projections of ice discharge are plagued with dramatic uncertainties. Likely, these uncertainties are largest for Greenland's high-velocity outlet glaciers, which are expected to contribute the most to changes in future sea level.

In order to illustrate how perturbations to the different fields may compound during an extreme change in climate, we include results from a sampling experiment where B_r, α, and SMB are sampled at the same time (Figure 5). For instance, during July of 2012, the percentage of the Greenland surface exposed to melt was the largest in recorded history [*Nghiem et al.*, 2012], extending to over 97% of the ice sheet. In a warming climate, the frequency of such an event is expected to increase, leading to the presence of more runoff. Increased runoff may enter the subglacial hydrological system, leading to local velocity increases due to processes like lubrication of the bed [*Zwally et al.*, 2002; *Tedesco et al.*, 2012] or heating of the ice due to the refreeze of surface runoff at depth [*Phillips et al.*, 2013; *Bell et al.*, 2014]. In our extreme example, α and SMB are separately responsible for over 120% uncertainty in mass flux in the northern branch of the NEGIS (i.e., Gate NB), and B_r is responsible for a 7% mass flux uncertainty. Sampled together, however, these errors are responsible for 188% uncertainty in mass flux. The resulting uncertainty is significant: at one extreme, it represents a complete shutdown of the northern branch of the NEGIS, and on the other extreme, it represents over a doubling of mass flux. Sensitivity maps show that ice flow in the northern branch of the NEGIS is most strongly connected with ice flow in 79North but also that it is related to flow in the main branch of the ice stream. If the northern branch were to shut down, results suggest that it would provide less ice to 79North, and the main branch would speed up to compensate for the deficit. This extreme forcing provides another example of the significant mass flux uncertainties that would be associated with a changing climate. Here we find that climate-driven processes can enhance drawdown of upstream ice and lead to an overall thinning of the ice sheet. On the other hand, if the northern branch were to discharge more mass, the main branch would slow down, leading to overall thickening.

The extreme results presented in Figure 5 also illustrate that simulated NEGIS mass fluxes are robust and well behaved, in agreement with *Schlegel et al.* [2013]. In addition, we find that these mass fluxes are very sensitive to errors in α and fairly sensitive to errors in B_r and SMB, especially near the margins. We estimate that outlet discharge uncertainty due to B_r is 3.3 Gt/yr (13% for 79North, 14% Zachariæ Isstrøm, and 2% for Storstrømmen glacier). These discharge uncertainties are less than those associated with a 20% error in

basal drag coefficient (5.7 Gt/yr) or those associated with SMB (4.5 Gt/yr) but more than those associated with a 5% error in the basal drag coefficient (1.4 Gt/yr). Comparatively, we estimate uncertainties due to errors in B_g to be the least significant, responsible for a NEGIS discharge uncertainty of only 0.7 Gt/yr. These results confirm that since ice flow is so sensitive to α, it is an ideal parameter for inversion. Considering that basal drag is such an important parameter in terms of simulating ice flow in a dynamically active area such as the NEGIS, we find that the lack of knowledge about ice sheet basal conditions is a significant shortcoming in the field of ice sheet modeling. The transient evolution of the hydrological system, especially in terms of the subglacial routing and refreezing of runoff, is largely uncertain, yet critically important for determining an ice sheet's sensitivity to climate. Indeed, mass flux may be well behaved because this study does not consider positive feedback associated with transient processes that may play an important role in outlet glacier acceleration (e.g., meltwater hydrology or changes to calving front and grounding line positions). Better representation of these processes is absolutely necessary in order to improve the predictability of ice flow models.

6. Conclusion

In this study, we simulate NEGIS ice flow from 1989 to 2010 and use uncertainty quantification tools to investigate how errors in boundary conditions compare to the influence of climate forcing on the ice flow in Northeast Greenland. Using sampling techniques, we estimate that outlet discharge uncertainty due to geothermal heat flux effects on the ice viscosity parameter is 2.6% or 0.7 Gt/yr. This estimate is less than the 5.7 Gt/yr (19.8%) uncertainty associated with a 20% error in the basal drag coefficient and less than the 3.3 Gt/yr (11.6%) uncertainty associated with additional changes in the ice viscosity parameter due to surface meltwater subglacial drainage and refreeze. In comparison, we estimate that SMB errors are responsible for a NEGIS total outlet discharge uncertainty of 4.5 Gt/yr. Overall, we find that geothermal heat flux has a less significant effect on decadal-scale forward simulations of the NEGIS than do climate-driven transient processes, especially for ice sheet models that are spunup using inversion techniques. Ice flow is generally so sensitive to the choice of basal drag coefficient that most errors associated with geothermal heat flux will be compensated for by the inversion and will be encompassed in the resulting α field. This make α an ideal parameter for inversion but also highlights a critical gap in our knowledge when it comes to the basal conditions of an ice sheet, especially since basal drag is such a significant parameter for flow in a dynamically active area such as the NEGIS. Past results that indicate realistic errors in SMB, on the other hand, are indeed capable of altering flow, especially in a high-velocity flow regime. Thus, care should be taken in understanding the particular climate forcing used in ice flow models, including spatial variations and associated errors, as well as the transient hydrological processes associated with climate warming. We find that the errors associated with such processes, including enhancement of basal drag and the effects of cryohydrologic warming, are also capable of altering ice discharge, yet they are not well defined or understood. In the future, such errors must be quantified in order to accurately assess the uncertainties in ice sheet model projections.

Acknowledgments

This work was performed at the California Institute of Technology's Jet Propulsion Laboratory under a contract with the National Aeronautics and Space Administration's Modeling, Analysis, and Prediction (MAP) Program; Cryosphere Program; and President's and Director's Fund Program. The authors would like to acknowledge the data provided by the National Snow and Ice Data Center DAAC, University of Colorado, Boulder, CO, Operation IceBridge, as well as CReSIS data generated from NSF grant ANT-0424589 and NASA grant NNX10AT68G [*Gogineni*, 2012]. They would also like to thank three anonymous reviewers for their suggestions and comments which greatly aided in the improvement of this manuscript.

References

Bales, R. C., Q. Guo, D. Shen, J. R. McConnell, G. Du, J. F. Burkhart, V. B. Spikes, E. Hanna, and J. Cappelen (2009), Annual accumulation for Greenland updated using ice core data developed during 2000-2006 and analysis of daily coastal meteorological data, *J. Geophys. Res.*, *114*, D06116, doi:10.1029/2008JD011208.

Bartholomew, I., P. Nienow, D. Mair, A. Hubbard, M. A. King, and A. Sole (2010), Seasonal evolution of subglacial drainage and acceleration in a Greenland outlet glacier, *Nat. Geosci.*, *3*(6), 408–411, doi:10.1038/NGEO863.

Bell, R. E., K. Tinto, I. Das, M. Wolovick, W. Chu, T. T. Creyts, N. Frearson, A. Abdi, and J. D. Paden (2014), Deformation, warming and softening of Greenland's ice by refreezing meltwater, *Nat. Geosci.*, *7*(7), 497–502, doi:10.1038/ngeo2179.

Box, J. E. (2013), Greenland ice sheet mass balance reconstruction. Part II: Surface mass balance (1840-2010), *J. Clim.*, *26*(18), 6974–6989, doi:10.1175/JCLI-D-12-00518.1.

Box, J. E., et al. (2013), Greenland ice sheet mass balance reconstruction. Part I: Net snow accumulation (1600-2009), *J. Clim.*, *26*(11), 3919–3934, doi:10.1175/JCLI-D-12-00373.1.

Burgess, E. W., R. R. Forster, J. E. Box, E. Mosley-Thompson, D. H. Bromwich, R. C. Bales, and L. C. Smith (2010), A spatially calibrated model of annual accumulation rate on the Greenland Ice Sheet (1958-2007), *J. Geophys. Res.*, *115*, F02004, doi:10.1029/2009JF001293.

Cuffey, K., and W. S. B. Paterson (2010), *The Physics of Glaciers*, 4th ed., Elsevier, Oxford, U. K.

Dahl-Jensen, D., et al. (2013), Eemian interglacial reconstructed from a Greenland folded ice core, *Nature*, *493*(7433), 489–494, doi:10.1038/nature11789.

Dansgaard, W., et al. (1993), Evidence for general instability of past climate from a 250-kyr ice-core record, *Nature*, *364*(6434), 218–220, doi:10.1038/364218a0.

Eldred, M. S., et al. (2008), DAKOTA, a multilevel parallel object-oriented framework for design optimization, parameter estimation, uncertainty quantification, and sensitivity analysis, Version 4.2 User's Manual, *Tech. Rep. SAND 2006-6337*, Sandia Natl. Lab., Albuquerque, N. M.

Enderlin, E. M., I. M. Howat, S. Jeong, M.-J. Noh, J. H. van Angelen, and M. R. van den Broeke (2014), An improved mass budget for the Greenland ice sheet, *Geophys. Res. Lett.*, *41*, 866–872, doi:10.1002/2013GL059010.

Ettema, J., M. R. van den Broeke, E. van Meijgaard, W. J. van de Berg, J. L. Bamber, J. E. Box, and R. C. Bales (2009), Higher surface mass balance of the Greenland Ice Sheet revealed by high-resolution climate modeling, *Geophys. Res. Lett.*, *36*, L12501, doi:10.1029/2009GL038110.

Fahnestock, M., I. Joughin, T. Scambos, R. Kwok, W. Krabill, and S. Gogineni (2001), Ice stream related patterns of ice flow in the interior of northeast Greenland, *J. Geophys. Res.*, *106*, 34,035–34,045.

Fausto, R., A. Ahlstrom, D. Van As, S. Johnsen, P. L. Langen, and K. Steffen (2009), Improving surface boundary conditions with focus on coupling snow densification and meltwater retention in large-scale ice-sheet models of Greenland, *J. Glaciol.*, *55*(193), 869–878.

Fox Maule, C., M. E. Purucker, and N. Olsen (2009), Inferring magnetic crustal thickness and geothermal heat flux from crustal magnetic field models, *Tech. Rep. 09-09*, Danish Meteorol. Inst., Copenhagen, Den. [Available at http://www.dmi.dk/dmi/dkc09-09.pdf.]

Gardner, A. S., et al. (2013), A reconciled estimate of glacier contributions to sea level rise: 2003 to 2009, *Science*, *340*(6134), 852–857, doi:10.1126/science.1234532.

Glen, J. (1955), The creep of polycrystalline ice, *Proc. R. Soc. A*, *228*(1175), 519–538.

Gogineni, P. (2012), CReSIS RDS Data, Lawrence, Kans., Digital Media. [Available at http://data.cresis.ku.edu/.]

Greenland Ice-Core Project (Grip) Members (1993), Climate instability during the last interglacial period recorded in the grip ice core, *Nature*, *364*(6434), 203–207.

Greve, R. (2005), Relation of measured basal temperatures and the spatial distribution of the geothermal heat flux for the Greenland ice sheet, *Ann. Glaciol.*, *42*, 424–432.

Greve, R., and K. Hutter (1995), Polythermal three-dimensional modelling of the Greenland ice sheet with varied geothermal heat flux, *Ann. Glaciol.*, *21*, 8–12.

Hanna, E., P. Huybrechts, K. Steffen, J. Cappelen, R. Huff, C. Shuman, T. Irvine-Fynn, S. Wise, and M. Griffiths (2008), Increased runoff from melt from the Greenland Ice Sheet: A response to global warming, *J. Clim.*, *21*(2), 331–341, doi:10.1175/2007JCLI1964.1.

Hendrickson, B., and R. Leland (1995), The Chaco user's guide, version 2.0, *Tech. Rep. SAND-95-2344*, Sandia National Laboratories, Albuquerque, N. M.

Holland, D., R. Thomas, B. De Young, M. Ribergaard, and B. Lyberth (2008), Acceleration of Jakobshavn Isbrae triggered by warm subsurface ocean waters, *Nat. Geosci.*, *1*(10), 659–664, doi:10.1038/ngeo316.

Intergovernmental Panel on Climate Change (2013), Summary for policymakers, in *Climate Change 2013: The Physical Science Basis. Contribution of Working Group I to the Fifth Assessment Report of the Intergovernmental Panel on Climate Change*, edited by T. F. Stocker et al., pp. 1–30, Cambridge Univ. Press, Cambridge, U. K.

Joughin, I., M. Fahnestock, D. MacAyeal, J. Bamber, and P. Gogineni (2001), Observation and analysis of ice flow in the large Greenland ice stream, *J. Geophys. Res.*, *106*(D24), 34,021–34,034.

Khan, S. A., et al. (2014), Sustained mass loss of the northeast Greenland ice sheet triggered by regional warming, *Nat. Clim. Change*, *4*(4), 292–299, doi:10.1038/nclimate2161.

Larour, E., M. Morlighem, H. Seroussi, J. Schiermeier, and E. Rignot (2012a), Ice flow sensitivity to geothermal heat flux of Pine Island Glacier, Antarctica, *J. Geophys. Res.*, *117*, F04023, doi:10.1029/2012JF002371.

Larour, E., J. Schiermeier, E. Rignot, H. Seroussi, M. Morlighem, and J. Paden (2012b), Sensitivity analysis of Pine Island Glacier ice flow using ISSM and DAKOTA, *J. Geophys. Res.*, *117*, F02009, doi:10.1029/2011JF002146.

Larour, E., H. Seroussi, M. Morlighem, and E. Rignot (2012c), Continental scale, high order, high spatial resolution, ice sheet modeling using the Ice Sheet System Model (ISSM), *J. Geophys. Res.*, *117*, F01022, doi:10.1029/2011JF002140.

MacAyeal, D. (1989), Large-scale ice flow over a viscous basal sediment: Theory and application to ice stream B, Antarctica, *J. Geophys. Res.*, *94*(B4), 4071–4087.

MacAyeal, D. (1993), Binge/Purge oscillations of the Laurentide ice-sheet as a cause of the North-Atlantic's Heinrich events, *Paleoceanography*, *8*(6), 775–784.

Morlighem, M., E. Rignot, H. Seroussi, E. Larour, H. Ben Dhia, and D. Aubry (2010), Spatial patterns of basal drag inferred using control methods from a full-Stokes and simpler models for Pine Island Glacier, West Antarctica, *Geophys. Res. Lett.*, *37*, L14502, doi:10.1029/2010GL043853.

Morlighem, M., E. Rignot, J. Mouginot, H. Seroussi, and E. Larour (2014), High-resolution ice thickness mapping in South Greenland, *Ann. Glaciol.*, *55*(67), 64–70, doi:10.3189/2014AoG67A088.

Nghiem, S. V., D. K. Hall, T. L. Mote, M. Tedesco, M. R. Albert, K. Keegan, C. A. Shuman, N. E. DiGirolamo, and G. Neumann (2012), The extreme melt across the Greenland ice sheet in 2012, *Geophys. Res. Lett.*, *39*, L20502, doi:10.1029/2012GL053611.

Nowicki, S., et al. (2013), Insights into spatial sensitivities of ice mass response to environmental change from the SeaRISE ice sheet modeling project II: Greenland, *J. Geophys. Res.*, *118*, 1025–1044, doi:10.1002/jgrf.20076.

Paterson, W. (1994), *The Physics of Glaciers*, 3rd ed., Pergamon Press, Oxford, London and New York.

Pfeffer, W., M. Meier, and T. Illangasekare (1991), Retention of Greenland Runoff by Refreezing: Implications for projected future sea-level rise, *J. Geophys. Res.*, *96*(C12), 22,117–22,124, doi:10.1029/91JC02502.

Phillips, T., H. Rajaram, and K. Steffen (2010), Cryo-hydrologic warming: A potential mechanism for rapid thermal response of ice sheets, *Geophys. Res. Lett.*, *37*, L20503, doi:10.1029/2010GL044397.

Phillips, T., H. Rajaram, W. Colgan, K. Steffen, and W. Abdalati (2013), Evaluation of cryo-hydrologic warming as an explanation for increased ice velocities in the wet snow zone, Sermeq Avannarleq, West Greenland, *J. Geophys. Res. Earth Surf.*, *118*, 1241–1256, doi:10.1002/jgrf.20079.

Pollack, H., S. Hurter, and J. Johnson (1993), Heat flow from the Earth's interior: Analysis of the global data set, *Rev. Geophys.*, *31*, 267–280, doi:10.1029/93RG01249.

Rignot, E., and J. Mouginot (2012), Ice flow in Greenland for the International Polar Year 2008-2009, *Geophys. Res. Lett.*, *39*, L11501, doi:10.1029/2012GL051634.

Rignot, E., J. E. Box, E. Burgess, and E. Hanna (2008), Mass balance of the Greenland ice sheet from 1958 to 2007, *Geophys. Res. Lett.*, *35*, L20502, doi:10.1029/2008GL035417.

Rignot, E., M. Koppes, and I. Velicogna (2010), Rapid submarine melting of the calving faces of West Greenland glaciers, *Nat. Geosci.*, *3*(3), 187–191, doi:10.1038/ngeo765.

Rogozhina, I., J. Hagedoorn, M. Martinec, K. leming, O. Soucek, R. Greve, and M. Thomas (2012), Effects of uncertainties in the geothermal heat flux distribution on the Greenland Ice Sheet: An assessment of existing heat flow models, *J. Geophys. Res.*, *117*, F02025, doi:10.1029/2011JF002098.

Sasgen, I., M. van den Broeke, J. L. Bamber, E. Rignot, L. S. Sorensen, B. Wouters, Z. Martinec, I. Velicogna, and S. B. Simonsen (2012), Timing and origin of recent regional ice-mass loss in Greenland, *Earth Planet. Sci. Lett.*, *333*, 293–303, doi:10.1016/j.epsl.2012.03.033.

Scambos, T., and T. Haran (2002), An image-enhanced DEM of the Greenland ice sheet, *Ann. Glaciol.*, *34*, 291–298, doi:10.3189/172756402781817969.

Schenk, T., and B. Csatho (2012), A new methodology for detecting ice sheet surface elevation changes from laser altimetry data, *IEEE Trans. Geosci. Remote Sens.*, *50*(9), 3302–3316, doi:10.1109/TGRS.2011.2182357.

Schlegel, N.-J., E. Larour, H. Seroussi, M. Morlighem, and J. E. Box (2013), Decadal-scale sensitivity of Northeast Greenland ice flow to errors in surface mass balance using ISSM, *J. Geophys. Res. Earth Surf.*, *118*, 667–680, doi:10.1002/jgrf.20062.

Schoof, C. (2010), Coulomb friction and other sliding laws in a higher-order glacier flow model, *Math. Models Methods Appl. Sci.*, *20*(1), 157–189, doi:10.1142/S0218202510004180.

Seroussi, H., M. Morlighem, E. Rignot, E. Larour, D. Aubry, H. Ben Dhia, and S. S. Kristensen (2011), Ice flux divergence anomalies on 79north Glacier, Greenland, *Geophys. Res. Lett.*, *38*, L09501, doi:10.1029/2011GL047338.

Seroussi, H., M. Morlighem, E. Rignot, A. Khazendar, E. Larour, and J. Mouginot (2013), Dependence of century-scale projections of the Greenland ice sheet on its thermal regime, *J. Glaciol.*, *59*(218), 1024–1034, doi:10.3189/2013JoG13J054.

Shapiro, N., and M. Ritzwoller (2004), Inferring surface heat flux distributions guided by a global seismic model: Particular application to Antarctica, *Earth Planet. Sci. Lett.*, *223*(1–2), 213–224, doi:10.1016/j.epsl.2004.04.011.

Swiler, L. P., and G. D. Wyss (2004), A User's Guide to Sandia's Latin Hypercube Sampling Software: LHS UNIX Library/Standalone Version, *Tech. Rep. SAND2004-2439*, Sandia Natl. Lab., Albuquerque, N. M.

Tedesco, M., M. Luthje, K. Steffen, N. Steiner, X. Fettweis, I. Willis, N. Bayou, and A. Banwell (2012), Measurement and modeling of ablation of the bottom of supraglacial lakes in western Greenland, *Geophys. Res. Lett.*, *39*, L02502, doi:10.1029/2011GL049882.

van den Broeke, M., J. Bamber, J. Ettema, E. Rignot, E. Schrama, W. J. van de Berg, E. van Meijgaard, I. Velicogna, and B. Wouters (2009), Partitioning recent Greenland mass loss, *Science*, *326*(5955), 984–986, doi:10.1126/science.1178176.

Walter, J. I., J. E. Box, S. Tulaczyk, E. E. Brodsky, I. M. Howat, Y. Ahn, and A. Brown (2012), Oceanic mechanical forcing of a marine-terminating Greenland glacier, *Ann. Glaciol.*, *53*(60), 181–192, doi:10.3189/2012AoG60A083.

Wouters, B., J. L. Bamber, M. R. van den Broeke, J. T. M. Lenaerts, and I. Sasgen (2013), Limits in detecting acceleration of ice sheet mass loss due to climate variability, *Nat. Geosci.*, *6*(8), 613–616, doi:10.1038/ngeo1874.

Zwally, H. J., W. Abdalati, T. Herring, K. Larson, J. Saba, and K. Steffen (2002), Surface melt-induced acceleration of Greenland ice-sheet flow, *Science*, *297*(5579), 218–222, doi:10.1126/science.1072708.